

Autonomous Science during Large-Scale Robotic Survey

David R. Thompson*, David S. Wettergreen, Francisco J. Calderón Peralta†

The Robotics Institute, Carnegie Mellon University
5000 Forbes Ave, Pittsburgh, PA 15213, USA

David.R.Thompson@jpl.nasa.gov, dsw@ri.cmu.edu, francisco.calderon@pochcorp.com

Abstract

Today’s planetary exploration robots rarely travel beyond the yesterday imagery. However, advances in autonomous mobility will soon permit single-command site surveys of multiple kilometers. Here scientists cannot see the terrain in advance and explorer robots must navigate and collect data autonomously. Onboard science data understanding can improve these surveys with image analysis, pattern recognition, learned classification and information-theoretic planning. We report on field experiments near Amboy Crater, California that demonstrate fundamental capabilities for autonomous surficial mapping of geologic phenomena with a visible near-infrared spectrometer. We develop an approach to “science on the fly” that adapts the robot’s exploration using collected instrument data. We demonstrate feature detection and visual servoing to acquire spectra from dozens of targets without human intervention. The rover interprets spectra onboard, learning spatial models of science phenomena that guide it toward informative areas. It discovers spatial structure (correlations between neighboring regions) and cross-sensor structure (correlations between different scales). The rover uses surface observations to reinterpret satellite imagery and improve exploration efficiency.

1 Introduction

In recent decades planetary exploration has benefited from dramatic mobility improvements; orbital flybys preceded soft landings and eventually mobile rover platforms. The Mars Exploration Rovers regularly travel tens of meters per day with stereo terrain analysis and have demonstrated autonomous navigation for even longer traverses (Maimone et al., 2007; Carsten et al., 2007). Terrestrial analogue tests have demonstrated single-command traverses on kilometer scales (Fong et al., 2008; Thompson and Wettergreen, 2008; Wettergreen et al., 2008). Scientists can use these over-the-horizon modes to quickly characterize large areas and visit multiple geologic units between communications opportunities (Wettergreen et al., 2005; Cabrol et al., 2007). This promises significant benefits for our understanding of Mars and other planetary bodies. However communication will remain sporadic and much of the terrain these rovers pass through might never be seen by humans.

Onboard science data analysis can play a role in such operations. First, it can recognize science features for opportunistic data collection. The rover can identify important features and deploy targeted instruments

* Now at the Jet Propulsion Laboratory, California Institute of Technology, 4800 Oak Drive, M/S 306-463, Pasadena, CA 91109, USA

† Now at Poch Applied Technologies, Alcántara 464, Santiago, Chile



Figure 1: The Zoë rover (Wettergreen et al., 2005) at Amboy Crater. Key terrain features include basalt mounds, areas of hard sediment, and scattered basalt cobbles visible in the foreground.

without direct supervision (Chien et al., 2005; Castaño et al., 2007; Estlin et al., 2010; Pugh et al., 2010b). Second, onboard analysis can choose traverse paths to maximize science utility. It can prioritize informative locations such as local anomalies, bypassing redundant measurements and quickly surveying large areas (McGuire et al., 2005; Fink, 2006). Finally, onboard science analysis can select or summarize data for bandwidth-restricted downlink opportunities (Thompson et al., 2008; Hayden et al., 2010).

This article describes science autonomy during a rover site survey at Amboy Crater, California (Figure 1). The survey aims to build an accurate geologic map of surface material under strict time constraints. We develop an approach to “science on the fly” in which the rover adapts its activities based on collected data. This requires several specific capabilities:

- Adaptive instrument control: the ability to recognize features of interest and perform targeted data collection to acquire high-quality measurements.
- Science data interpretation: classification or statistical models that make meaningful inferences about measurement data.
- Information optimal decision making: the ability to change sensor deployment or traverse plans to maximize information about the phenomena of interest.

We demonstrate these capabilities with two field experiments. The first involves science target detection and instrument control using a visible near-infrared reflectance spectrometer. Here the rover collects representative spectra from targets it finds along its traverse path. The detection and targeting does not require that operators see the terrain in advance. The rover uses these measurements to build a map of rocks and soil.

Later experiments generalize this concept to large-scale adaptive path planning. Here the rover reinterprets collected spectrometer data on the fly and learns a Gaussian process spatial model of the environment. It

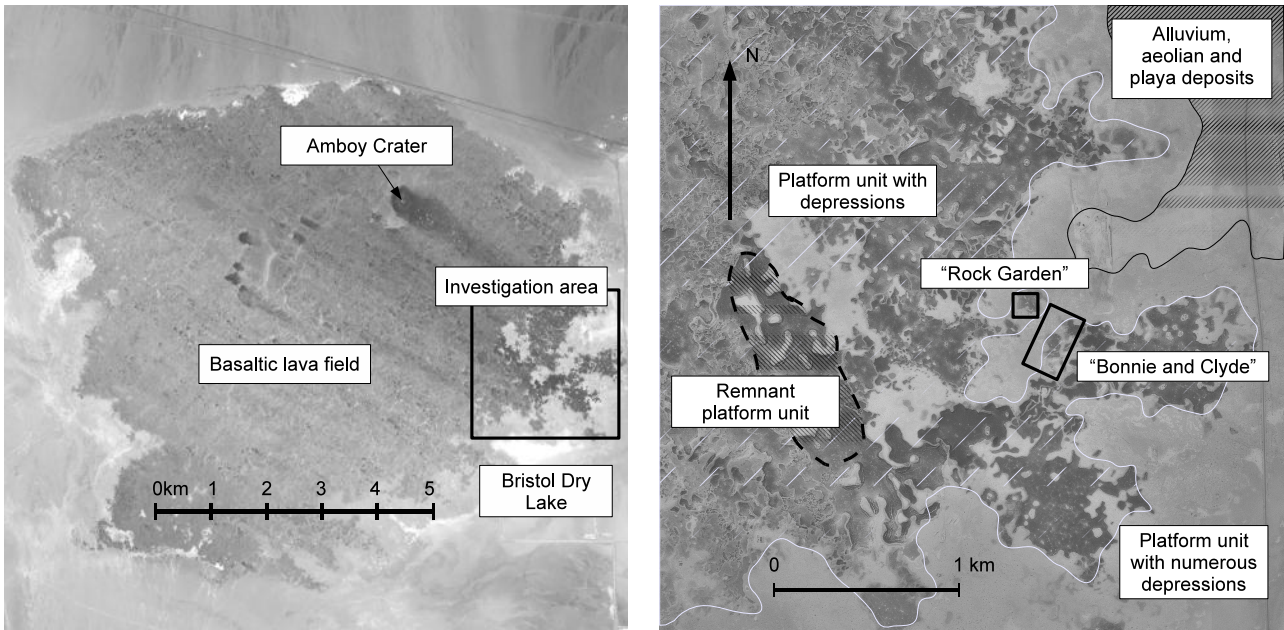


Figure 2: Left: An ASTER image (band 1, 520-600 nm) shows the Amboy Crater lava field. Right: Geologic maps from Hatheway (Hatheway, 1971; Greeley and Iversen, 1978). The background image is a USGS Digital Orthophoto Quadrangle product.

uses this map to choose paths that maximize information gain and satisfy mission time constraints. These navigation decisions are sensitive to discovered correlations across locations and between sensors. The method generates kilometer-scale maps of surface material in sub-hour timeframes.

1.1 Amboy Crater Lava Field

Amboy Crater is a volcanic cinder cone located in California's Mojave Desert; Figure 2 shows orbital views from the ASTER instrument. The cone is surrounded by 70km² of basaltic flows composed mostly of layered vesicular pahoehoe lava deposited in flat-topped platform units. The surface resembles a Viking landing site which makes Amboy a reasonable analogue to Mars, and the basalt is compositionally similar to the Moon (Greeley and Iversen, 1978). It has previously hosted tests of rover operations (Christian et al., 1997), penetrator sensors, and wheeled mobility (Winterholler et al., 2005).

The basalt units are oldest on the Eastern edge of the lava field (Greeley and Iversen, 1978), where they form an abrupt contact against the Bristol Lake Playa with broken edges characterized by distinctive heterogeneous morphology and many circular "collapse depressions" (Figure 2). Our experiments survey a diverse area composed of several geologic units (Figure 2, Left). Figure 2 (Right) shows unit boundaries identified by Hatheway and reprinted in Greeley *et al* (Hatheway, 1971; Greeley and Iversen, 1978). The platform edges show prominent erosion with aeolian sediment deposits punctuated by distinctive basalt mounds varying in height from surface level to approximately 3 meters (Figure 1).

Our experiments use spectroscopy to characterize the geologic diversity of the platform units. Relevant issues include the nature and extent of the basalt mounds, the relationship between orbital imagery and platform composition, and the morphology of the basalt features at different locations in the flow. A single field experiment cannot resolve all these issues but it does motivate objectives for a technology demonstration. Specifically, the rover should have sufficient mobility to survey multiple platforms on a single command. It must carry an instrument package capable of characterizing the key surface materials, and automatically map the distribution of basalt in the explored region.



Figure 3: The spectrometer’s foreoptic mounts rigidly to the stereo rig atop Zoë’s mast. Fiber-optic cable carries light reflected from objects in the 1° field of view to detector arrays inside the rover. The stereo cameras allow the rover to localize detected geologic features.

1.2 Rover Platform and Instruments

We use the exploration robot Zoë (Figure 1) developed at Carnegie Mellon University for long-distance traverse (Cabrol et al., 2007; Wettergreen et al., 2005). The rover is 2 meters long and can move up to 1 meter per second under solar power. Zoë’s front and rear axles pivot freely, and are steered by the differential velocity of the four wheels (Wagner et al., 2005). It drives variable-radius arcs and reliably surmounts obstacles of up to 25 centimeters in height.

Zoë’s science suite includes a calibrated 60cm-baseline stereo camera rig analogous to the science PanCams on the Mars Exploration Rovers (Squyres et al., 2003). It sits at 2m height on an actuated pan-tilt base with full 360° rotation (Figure 3). These science cameras have 60° fields of view and capture 1280×960 pixel images.

Zoë also carries an ASD FieldSpec Pro (ASD, Inc., 2010), a visible near-infrared reflectance spectrometer that can analyze distant targets under passive solar illumination. The spectrometer samples at 1.4nm intervals in the 350 – 1050nm range, and 2nm intervals in the SWIR 1000 – 2500nm range. Its objective *foreoptic* lens is fixed to the pan-tilt servo unit on the rover mast (Figure 3). The foreoptic’s field of view forms a 1° sensing cone in space. The spectrometer clearly distinguishes basalt and sediment materials (Figure 4). The basalt has a higher proportional reflectance in the short visible wavelengths and a lower reflectance overall. Varying densities of basalt produce mixtures of the two signals. The rover automatically compensates for changes in ambient illumination, renormalizing the spectrometer by aiming at a white reference target fixed to the deck. Calderón et al. give details of the automatic calibration procedure (Calderón et al., 2008).

1.3 Local Navigation and Terrain Evaluation

Our science on the fly experiments use a two-tier navigation strategy that bifurcates local path planning based on terrain from long range strategic planning based on science goals. The local path planner performs terrain evaluation with fixed mast-mounted navigation cameras for near-field stereopsis (Wettergreen et al., 2005; Wettergreen et al., 2008). The navigation cameras capture 320×240 pixel images which are processed into 3D point clouds at approximately 5 Hz. The mobility software (hereafter, the “Navigator”) fits planar patches to foreground locations. The height and orientation of each plane defines a traversability score (Figure 5).

The Navigator chooses safe drive arcs that guide the vehicle from one waypoint to the next. Each new waypoint requires a new traversability map with the waypoint as destination. The Navigator considers a

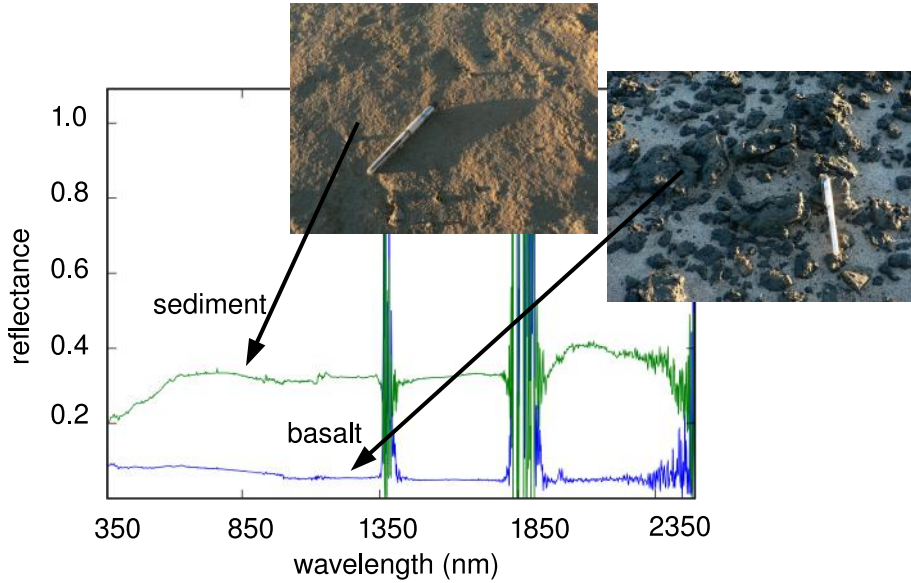


Figure 4: Spectra of basalt (bottom) and clay (top) at Amboy Crater under solar illumination. Atmospheric water absorption produces low signal-to-noise ratios in bands at 1350, 1850, and 2350 nanometers.

group of arcs and evaluates their traversability as well as distance to the goal, estimated using a D^* path planning algorithm (Singh et al., 2000; Maimone et al., 2007; Stentz and Hebert, 1995) and the terrain model. The Navigator updates the commanded steering angle and velocity at regular intervals. Wettergreen et al. describe the navigation system at length (Wettergreen et al., 2008).

In our exploration scenario, remote scientists use visible landmarks to estimate a start-of-day position. We simulate this by initializing rover position with an absolute GPS measurement. During the traverse the rover updates its position with dead reckoning. Planetary rovers could derive absolute heading data from celestial and solar navigation systems utilizing ephemeris calculations (Deans et al., 2005); an onboard magnetic compass emulates this capability with heading corrections at 5 Hz frequency. Wheel slip results in residual localization error ranging from 0 – 5% of distance traveled. One could further improve position estimation with techniques like visual odometry (Cheng et al., 2006).

2 Autonomous Rock Detection and Targeting

Science on the fly rests on a foundation of autonomous feature detection and instrument control. This involves detecting and localizing features, finding correspondences among multiple detections, controlling the instrument, and associating measurement data with the proper targets. Experiments at Amboy demonstrate these capabilities for rock features. Rocks are particularly informative features and the search for interesting rocks pervades planetary exploration. Rocks can carry unique mineralogical signatures and their transport suggests geologic changes. As discrete objects, rocks provide a well-defined test for target selection. This section describes a method that collects an average rate of one rock spectrum per two minutes of rover travel time.

Much previous research examines Single-Cycle Instrument Placement (SCIP) of contact spectrometers (P. Backes et al., 2005; Bajracharya et al., 2005; Madison, 2006; Huntsberger et al., 2005; Yoder and Seelinger, 2008; Maimone et al., 2007). Pedersen et al. extend this model to multiple targets (Pedersen et al., 2005). Our approach autonomously detects targets for follow-up remote sensing, similar to the Mars Rovers' AEGIS system (Estlin et al., 2010). It differs in that it analyzes traverse images while the rover is in motion, localizes

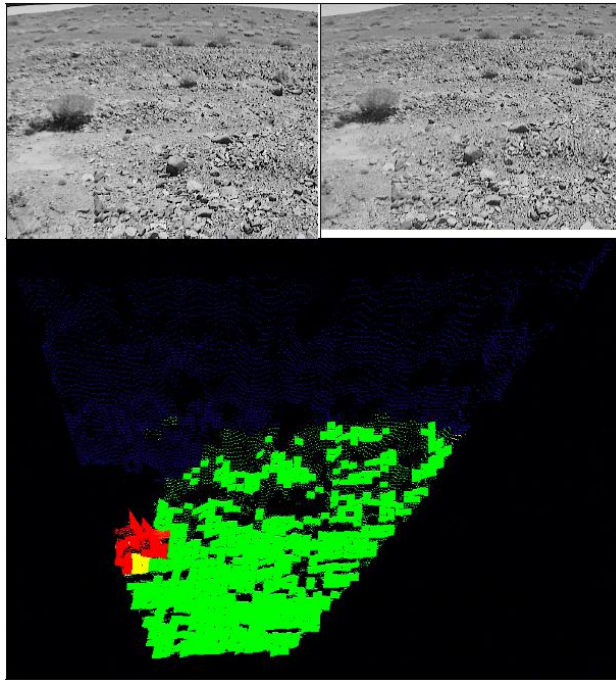


Figure 5: The rover navigator performs low-level hazard avoidance. Top: Left and right stereo images from navigation cameras. Bottom: Traversability model showing patches of terrain evaluated based on height and orientation. The red patch corresponds to an obstacle (here, a bush).

and tracks features over time, and resolves correspondence with previous detections to build a catalog of unique objects (Calderón et al., 2008). The rover periodically pauses its traverse and uses a visual servo procedure to target promising features (Calderón, 2007). The spectrometer targeting has a relatively high failure rate — over 50% in some cases due to the difficulty of identifying a clean target and aligning the 1° field of view — but the rover can initiate more targeting after a miss. This approach has allowed the robot to collect dozens of spectrometer measurements from a single user-issued traverse command. It compiles these spectra into a representative map for downlink.

2.1 Method

2.1.1 Spectrometer Profiling as an Operational Mode

Here we define a *spectrometer profiling* operational mode which collects representative spectra from rocks and soil along a rover transect. An operator command specifies a start location, a goal waypoint, and a time budget. During the traverse the rover alternates between a *travel* state for navigation and an *observe* state in which it stops to acquire spectra. In the *travel* state the rover drives to the next goal waypoint using the local navigator described in Section 1.3. Meanwhile the rover detects any rocks in forward-looking images, panning alternately to the left and right for coverage. The ongoing analysis estimates rocks’ absolute positions and inserts them into a database of geologic features. Figure 6 shows the flow of information between the three subtasks that handle data acquisition, image analysis, and navigation. Red components are interfaces to rover hardware.

The rover switches to an *observe* state when two conditions are satisfied: there must be at least one unmeasured rock within spectrometer range, and the traverse segment must retain sufficient time for a targeting sequence. Then the Navigator pauses and the rover begins spectrometer targeting. Each successful sequence produces a new spectrum which is uniquely associated with the correct rock in the database. A state

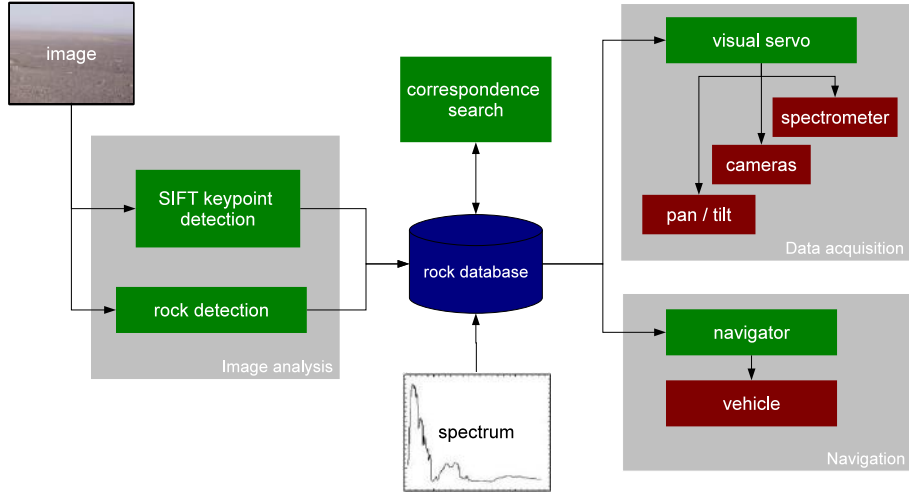


Figure 6: Components of feature tracking and spectrometer acquisition. The rock database contains a list of unique features and associated attributes.

flowchart for data acquisition and navigation modules appears in Figure 7.

The rock database is a relational database that associates the following information with each target: 1) a globally unique identifier index; 2) a global 3D position estimate in Earth-Centered-Earth-Fixed (ECEF) coordinates; 3) pixel-coordinate bounding boxes for each image in which the rock appears; 4) scale-invariant features for recognizing the rock in new images; 5) visible attributes of the rock, such as its size; and 6) the rock’s spectrum if available. We use Scale-Invariant Feature Transform (SIFT) descriptors (Lowe, 2004) to recognize old rocks. These descriptors’ appearances are preserved across small changes in perspective. SIFT correspondence matching ensures each physical feature has a single unique database entry.

2.1.2 Detecting Rock and Soil Features

Previous studies propose various rock detection strategies. Gulick *et al* find rocks by searching for terminator lines between light and shaded areas (Gulick et al., 2001). The Nomad platform uses cameras with color segmentation to identify dark rocks against an ice background (Wagner et al., 2001). Methods employing 3D geometry include the stereo techniques of Fox *et al.* and Pedersen *et al.* (Fox et al., 2002; Pedersen, 2002). These fit a simple parametric model to the terrain in order to identify objects that protrude above the surface. They perform best in environments with flat terrain and large rocks. Other detection strategies look for closed contours with edge detection such as *Rockfinder* (Castaño, 2006) and *Rockster* (Estlin et al., 2008). Fink et al. propose the segmentation-based Automated Global Feature Analyzer (Fink et al., 2008) to inform a multi-tier exploration system that can incorporate surface, aerial, and orbital components (Fink et al., 2005; Kean, 2010). Pugh et al. also use a segmentation-based approach to rock detection, and demonstrate follow-up camera observations on a rover analog (Pugh et al., 2010a; Pugh et al., 2010b). Recently the AEGIS system demonstrated contour-based rock detection at Mars when it ran onboard the Mars Exploration Rover “Opportunity” (Estlin et al., 2009; Estlin et al., 2010).

The Amboy experiments use a template-based approach to target detection. A Viola-Jones classifier evaluates all potential bounding boxes in the image at various scales for their probability of containing a target (Viola and Jones, 2001). It uses an integral image caching structure for fast feature extraction. A boosted cascade of decision trees classifies each candidate, computing only as many features as required to achieve sufficient classification certainty. We used this method for its ease of implementation and its speed of operation on full-resolution images. It offered reliable performance in our Amboy test scenario.

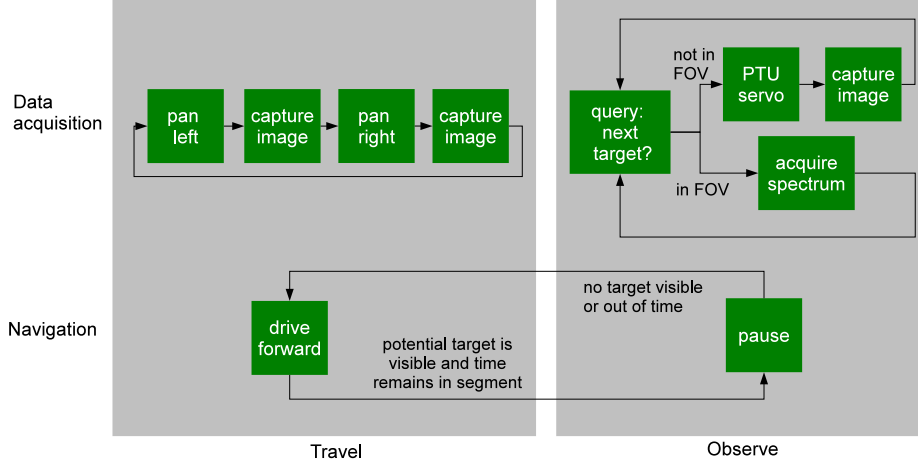


Figure 7: State model. The rover advances in a *travel* state whenever no time remains in its current segment or when there is no nearby target candidate in the database. In the *observe* state a visual servo loop tries to place the next target in the spectrometer field of view.

We augment the basic Viola - Jones strategy to exploit directed lighting. The distribution of possible rock appearances is multimodal due to the unknown direction of shadows and highlights. We capture this effect by imposing a constraint that the effective lighting direction be the same for all rocks within each image. This is a safe assumption since there is only ever a single significant point illumination source at infinity. The only unknown is the sun's direction, which we estimate independently for each new frame.

The implementation resembles a mixture of experts approach (Waterhouse, 1997); we train multiple classifiers that each specialize in a subset of illumination directions. Specifically we use a pair of parallel filter cascades where each is trained to recognize rocks illuminated from one of two sides. These simultaneous cascades compete to interpret each new image. If true positives are more likely than false positives then the detector with more returns has the better model of scene illumination. Thus, our rock detector uses results from the cascade that finds the most rocks. For example, in Figure 8 the system successfully identifies the right-lit model as the correct cascade. One can double the training data through mirroring (Viola and Jones, 2001) as long as each classifier is trained using a single effective lighting direction. For further detail and an evaluation on Mars images we refer the reader to previous work by Thompson *et al.* (Thompson and Castaño, 2007).

2.1.3 Cataloging Unique Objects and their Locations

Correspondence matching incorporates detected features into a catalog of unique objects and their physical locations. The system ignores detections less than 10cm in size (too small for accurate targeting), within 2m of the rover center (often affected by the rover body or its shadow), or that overlap with a larger bounding box by more than half of their area (duplicate detection). Figure 8 shows resulting targets with text indicating position estimates derived from point stereo (Hartley and Zisserman, 2004).

We use SIFT descriptors (Lowe, 2004) to establish correspondence between instances of the same rock in different views. The SIFT procedure identifies stable image points using unique descriptors that are well-preserved across slight changes in viewing position or illumination. Each rock in the database has associated SIFT keypoints taken from its bounding box. The rover recognizes old features by matching each new image's SIFT descriptors against this catalog. It estimates the physical location of each SIFT keypoint and uses a 1m search radius to seek potential database matches. We improve reliability by augmenting Lowe's SIFT matching criterion with a “backwards” comparison (Calderón et al., 2008). For each correspondence match we apply a similar search using the old SIFT descriptor as the query and the new image's SIFT descriptors as the search space. A valid correspondence match must be unique in both directions. A successful match

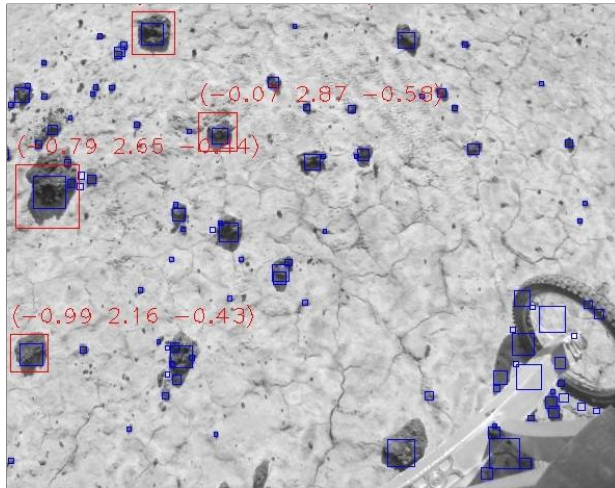


Figure 8: Detection result after filtering by rock size and distance. Large red bounding boxes are potential spectrometer targets, with numbers indicating rover-relative position estimates. Blue squares indicate SIFT keypoints for the correspondence search.

implies that the descriptor lies on a previously-detected target, and the database is updated with the rock’s visual attributes, position and associated descriptors. A newly-detected rock with no matches generates a new entry in the database.

Most rocks large enough to serve as spectrometer targets contain at least one stable keypoint descriptor (Figure 8). Because rocks do not fill their bounding boxes, keypoints on the edge or the ground can be accidentally included. For example, rock shadows have high-contrast borders that can generate SIFT features within the bounding box. Tracking shadows instead of the rock surface is an occasional failure mode. Depending on lighting conditions, rock spectra are weak or absent in approximately 20 – 40% of acquired spectra and out-of-rock SIFT features probably cause a significant portion of that error.

Two different methods estimate target position. Stereopsis generates a 3D estimate based on the centroid of a feature’s keypoints. Robust two-way matching finds keypoints appearing in both cameras. We compute a camera-relative position using a least-squares geometric reconstruction with a calibrated pinhole camera model and radial distortion (Hartley and Zisserman, 2004). Position estimation is consistent to about 5cm for rocks within spectrometer range. While the rover is moving, we assume planar terrain and known kinematics to approximate target position from a single image. The robot refines this rough estimate using stereo whenever it pauses for spectrum collection.

Targeting uses a two stage procedure. A feedforward step performs a rough targeting based on a kinematic model of the the pan/tilt mount and the most recent rock position estimate. Then a second feedback step refines the pointing with an iterative visual servoing approach. Both feedforward and feedback steps attempt to center the spectrometer field of view on the target for maximum coverage. Calderón provides additional details of the kinematic model (Calderón, 2007). In brief, the spectrometer is rigidly fixed to the stereo rig and calibrated to the left camera. Pointing the spectrometer at a target with known depth is equivalent to moving the mast pan/tilt until the target appears in the appropriate pixel of the image. This defines an error in visual space based on the current and desired target position. The system applies a simple visual servo (Hutchinson et al., 1996) with a proportional control law. It iterates until the error within the 1280×960 pixel frame falls below a 3 pixel threshold. The method can accurately target features for spectrum acquisition at ranges up to 5m.



Figure 9: The “rock garden” at Amboy Crater where spectrometer profile experiments were conducted.

2.1.4 Verifying Spectrometer Profile Performance

We performed several field trials to evaluate spectrometer profiling capabilities. In a flat location near Amboy Crater a basalt mound had eroded to the level of the base sediment (Figure 9). This left a scattering of rocks along a patch of ground approximately 50m × 50m. Clay predominated, but the scattered rocks up to 30cm in length were also visible. Here rock detection combined with visual servoing significantly improved the diversity and quality of collected spectra over blind targeting strategies.

We tested the spectrometer profiling system using 4 trials of a 50m transect. We mitigated inter-trial and between-trial illumination differences by testing at midday when shadows changed slowly. Atmospheric conditions such as cloud density varied somewhat across runs. The robot began each trial in the same starting location and initialized its position using differential GPS. Each trial lasted 40 minutes. The rover distributed this budget evenly to 10 segments of 5m length. It navigated forward from one intermediate waypoint to the next, rolling at a commanded velocity of 0.1m/s until a suitable target triggered a switch to the *observe* mode. It then paused and initiated spectrum collection.

We quantified targeting accuracy by manually identifying clear endmember examples of basalt and sediment for each trial. These permitted linear unmixing of the other collected spectra. We labeled those showing at least 50% basalt as a success. This threshold agreed qualitatively with a human visual interpretation. We compared system performance against data acquisition without rock detection, in which the robot held the pan/tilt unit at a fixed -30° declination and collected spectra at regular intervals. Slight perturbations of the start location (about 0.2m) ensured that the foreoptic’s field of view swept over different areas in each trial.

2.2 Spectrometer Profiling Results

Figure 10 shows the result of four test runs with approximately 50 spectrum collection attempts each. An attempt results in one of three end conditions: *lost*, *missed*, or *successful*. The *lost* condition occurs when the robot cannot find a conclusive match and fails to re-acquire a target during its 2 – 5 visual servo iterations. It aborts the attempt and progresses to the next target rock. The percentage of tracking sequences which run to completion appears in the middle column of Table 1; this reflects performance for tracking arbitrary SIFT features independent of rock detection accuracy. Factors leading to *lost* failures include loss of SIFT keypoints due to new illumination, rover pose, or shadows; similar SIFT descriptors in the database that prevent a confident match; or a SIFT keypoint that moves outside the camera’s field of view.

The *miss* condition occurs when a spectrum is collected but does not include basalt. The mixing coefficient of the basalt basis is less than the threshold, suggesting the rock did not subtend enough of the spectrometer field of view or the original rock detection was incorrect and there was no basalt present. The system collected

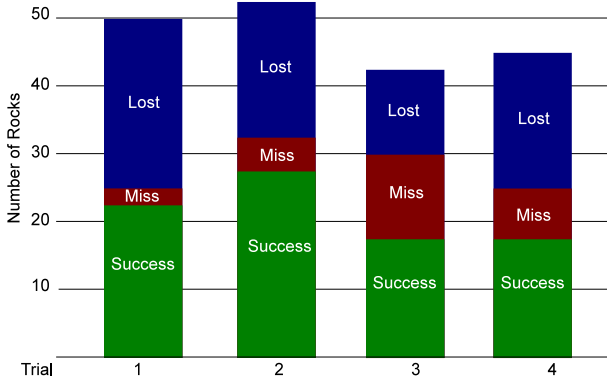


Figure 10: Result of spectrum collection by trial for each of four test runs. On average, the rover successfully collects a new spectrum every two minutes of travel time.

clean spectra at rates higher than 62% (Table 1, fourth column). Primary factors influencing the number of missed targets include: stereo errors; errors introduced by the ground plane assumption when stereo is not available; spurious rock detections; tracking visual features lying outside the rock (e.g. background or shadow); tracking visual features lying in the border of the rock (SIFT features are not guaranteed to be in the center of the rock); and SIFT mismatches during the tracking procedure.

We label an attempt a *success* when spectrometer tracking functions nominally and the unmixed signal reveals basalt. Figure 10 shows the distribution of success and failure cases for each trial; approximately 30 – 50% of the attempts are successful. The first two trials occurred consecutively on the same day. Lower performance in the first trial may be due to illumination changes. Trials 3 and 4 were also taken consecutively. We observe a slightly higher success tracking rate for trial 3; this may reflect slower illumination change due to higher solar zenith angle. In general tracking performance is over 55% when the light levels are favorable. We also evaluate rock detection independently through visual inspection, considering a detection successful if at least 50% of the bounding box contains a rock. Table 1 shows rock detection precision along with the other performance scores.

Figure 11 shows each trial’s detections against a georegistered Digital Orthophoto Quadrangle (DOQ) over-flight image. Small dots represent features in the database while larger circles show collected spectra. We also summarize each map with a rock density plot based on an inhomogeneous — that is, spatially varying — Poisson point process (Diggle, 2003). The point process density describes the mean number of rocks observed per unit area at any location in the map. The density in rocks per square meter facilitates a visual comparison of detection results across runs. It reveals a high degree of clustering in the distribution of rocks at the site. Three prominent areas early in the traverse have a particularly high concentration. The high-density areas appear in each trial except for run 2 which appears to be missing one of the modes. It is unclear whether this was due to changes in lighting conditions or the starting position of the rover. Several sparse clusters appear late in the traverse.

These results contrast sharply with three trials that did not use rock detection and targeting. These trials used periodic spectrum acquisition at a fixed angle; they never revealed any significant basalt signal. Therefore it is highly unlikely that a target would fall by chance into the spectrometer field of view during the periodic acquisition. Our pointing strategy significantly outperforms the blind method for the “Rock Garden” environment; each trial measures at least at 26 individual rocks over a 50m traverse lasting no longer than 40 minutes.

These experiments demonstrate real time feature detection and tracking for rover science on the fly. Integration of feature detection, tracking, targeting, and spectrum acquisition, could support autonomous spectroscopic mapping for kilometer-scale rover operations. The resulting map constitutes a bandwidth-

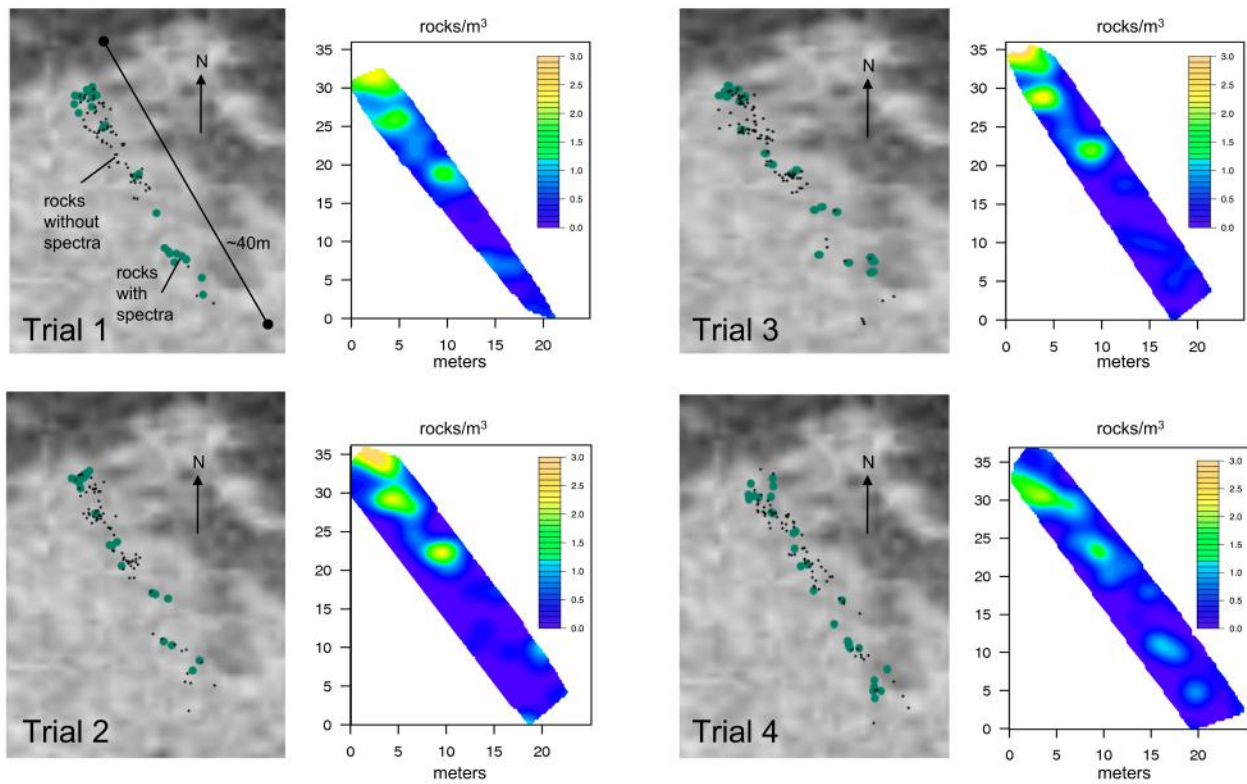


Figure 11: Left: Maps resulting from the spectrometer profile trials. Small black dots show rock features in the database, while large colored dots show collected spectra resulting from a completed visual servo procedure. Each run began in the upper-left corner and ended at a goal waypoint located 50 meters to the Southeast. Right: Density plots showing the number of detected rocks per square meter.

Targeted Sampling				Periodic Sampling		
Trial	Rock Detect.	Precision	Tracking Successes	Basalt Spectra	Trial	Basalt Spectra
1	332/361 (92.0%)		26/50 (52.0%)	22/26 (84.6%)	1	0/68 (0.0%)
2	249/280 (88.9%)		32/52 (61.5%)	27/33 (81.8%)	2	0/67 (0.0%)
3	280/296 (94.6%)		29/43 (67.4%)	18/29 (62.1%)	3	0/64 (0.0%)
4	299/340 (87.9%)		26/46 (56.5%)	17/26 (65.4%)		
Total	1160/1277 (90.8%)		113/191 (59.2%)	84/114 (73.7%)	Total	0/199 (0.0%)

Table 1: Details of Amboy Crater trials using targeted spectroscopy (Left) and conventional periodic sampling (Right).

efficient data product to describe traverse images and inform future data collection. These maps may still exhibit biases due to terrain or lighting so one should still be cautious in using them as a quantitative scientific measurement tool.

3 Intelligent Mapping with Spatial Models

Another key science on the fly capability involves using collected measurements to infer future observations. This section builds on automatic instrument control to enable kilometer-scale surveys that discern measurements’ spatial trends and correlations with remote sensing data. We treat site survey as a mapping task guided by principles of spatial experimental design. The objective is to construct a faithful spatial model of basalt density. This is tantamount to an active learning problem where the value of new data depends on the information it provides for the map.

The mapping objective reflects important elements of geologists’ field technique. Geologic interpretations must consider spatial context. They incorporate many observations into a holistic narrative of formation and alteration processes on large scales. Similarly, robots performing site survey could model spatial phenomena like geologic units, borders and the general correlations between neighboring locations. Identifying regions of homogeneity and change let them adapt data collection to spatial trends and anomalies. Second, geologic interpretations rely on multiple sensors at different scales (Fink et al., 2005; Furfaro et al., 2008; Furfaro et al., 2010). A single site survey might consider *in situ* inspection but also wide-coverage remote sensing data (Cabrol et al., 2007). Our adaptive mapping strategy incorporates both kinds of statistical inference (Figure 12). Spatial structure (Figure 12 Left) describes correlations between nearby samples, while cross-sensor structure (Figure 12 Right) captures relationships between orbital and surface measurements.

The Amboy system performs these inference tasks with a Gaussian process spatial model (Williams and Rasmussen, 1996). This generative model defines the probability of future results at candidate measurement locations. Zoë learns model parameters on the fly and uses its predictions for adaptive exploration. Optimal data collection actions maximize an experimental design criterion — in this case, expected information gain with respect to the map. Zoë plans survey paths that improve map fidelity while satisfying constraints on time resources and end-of-day locations. This demonstrates predictive mapping for science on the fly.

3.1 Intelligent Mapping

In our experiments, operators specify a total time budget, an end-of-day goal location, and a lateral offset defining a rectangular “safe area” in which the robot can travel freely. This scenario resembles the corridor exploration of Smith *et al* (Smith et al., 2007b; Smith et al., 2007a). The rover chooses intermediate waypoints that visit the most informative terrain subject to boundary limits and the end-of-day goal. We limit the search space by requiring the plan to progress further along the corridor with each step. The Navigator can travel backwards to avoid obstacles, but each successive waypoint must lie closer to the goal. During travel



Figure 12: Left: Spatial inference predicts observations using context from nearby measurements. Right: Cross-sensor inference predicts observations based on correlations with preexisting orbital images.

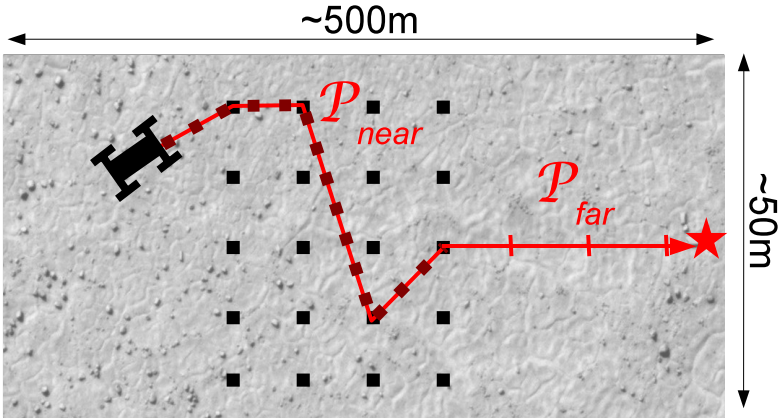


Figure 13: The rover travels forward toward a predefined end-of-day location. It chooses lateral waypoints to satisfy its near-term discretionary time budget while maximizing the information gain of observations along the path. P_{near} refers to the adaptive short-term path and P_{far} represents the remainder of the traverse.

the rover acquires spectra at 7 second intervals, and constructs a surficial map incorporating these data.

Our field experiments survey the “Bonnie and Clyde” site indicated in Figure 2. This is an area approximately 300m long and 100m wide, located in the East end of the Amboy lava field. It contains several distinct basalt platforms: a large flat area in the middle of the traverse corridor, and a dense basalt patch near the Northeast end. Clay predominates in other areas. Note that the pixel brightness of the remote images correlates somewhat with the basalt’s density. This correlation is unknown prior to the survey and we do not provide this information to the rover in advance.

3.2 Autonomous Spectrum Interpretation

A rover performing science on the fly must analyze collected spectra to extract meaningful geologic classifications. We represent the raw spectral signal at location x with a vector of wavelengths from $350 - 2500\mu\text{m}$, written $s(x) = [s_{350}(x), \dots, s_{2500}(x)]$. These experiments use only the interval from $350\mu\text{m}$ to $1000\mu\text{m}$, which avoids water absorption bands and captures the visible-spectrum diversity of the terrain. The absolute signal magnitude drifts quickly after calibration so we classify each spectrum using attributes of the waveshape. We

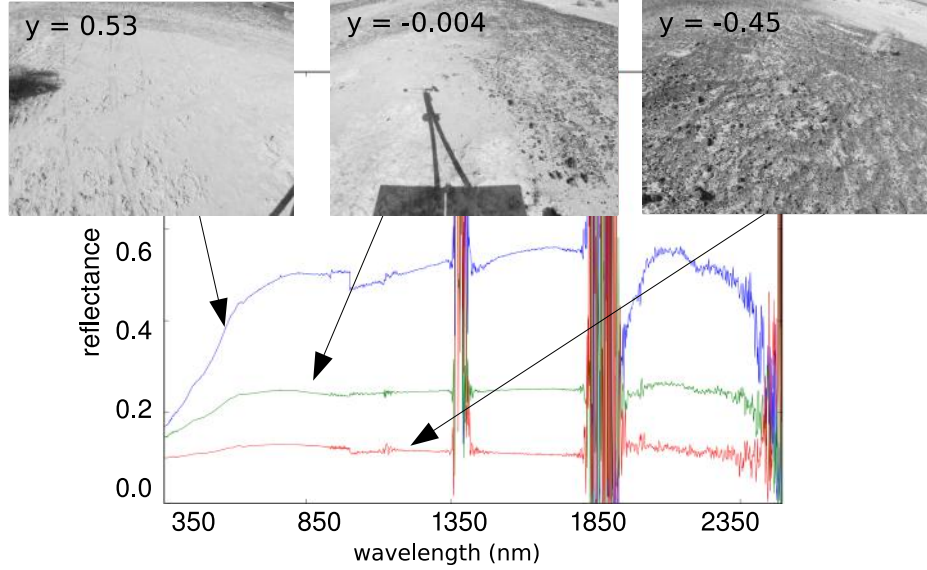


Figure 14: Mean and extreme observations from a traverse as determined by y values, i.e. the projection of each spectrum onto the first principal component. From left to right the images show pure sediment, a mixed scene, and dense basalt. The mast-mounted spectrometer views a small region near the center of the image frame.

aggregate values across multiple wavelengths into a five band histogram with edges at $350\mu\text{m}$, $450\mu\text{m}$, $550\mu\text{m}$, $700\mu\text{m}$, $850\mu\text{m}$, and $1000\mu\text{m}$. This produces the reduced signal $s_r(x) \in \mathbb{R}^5$. Rescaling this to the $[0, 1]$ interval produces an attribute vector $s_d(x)$ that is invariant to amplitude drift: $s_d(x) = \frac{s_r(x) - \min(s_r(x))}{\max s_r(x) - \min s_r(x)}$.

Reflectance spectra of macroscopic mixtures are generally linear combinations of the endmembers (Mustard et al., 1986). Here spectra describe a mixture of two physical materials (basalt and sediment) so their intrinsic dimensionality is approximately one. This corresponds to the first principal component of the $5D$ vector. During operations the system identifies the normalized principal eigenvector of the zero-meaned data's covariance matrix. A new signal $s_d(x)$ is analyzed by subtracting the original mean and projecting it onto this vector for a unitless measurement $y \in \mathbb{R}$ of basalt density. During travel the rover periodically recomputes the principal component and reprojects previous measurements to yield scalar observations $y_1 \dots y_n$. These values adapt to capture the basalt / sediment distinction without requiring a fixed mineral library (Ramsey and Christensen, 1998), pre-labeled examples (Bornstein and Castaño, 2005), or other *a priori* knowledge about materials the robot will encounter.

The dense basalt platforms of the “Bonnie and Clyde” region make precise targeting unnecessary. We fix the spectrometer at a -30° angle of declination throughout the traverse. Navigation images confirm that spectrometer data capture the distinction between terrain types. Figure 14 shows mean and extreme observations from a single traverse along with context images from the navigation cameras. The extreme values correspond to spectra of thick sediment (Left) and thick basalt (Right).

3.3 Gaussian Processes Models

The Amboy experiments produce maps that combine in situ spectra with the single-channel ASTER and USGS Digital Orthophoto Quadrangle (DOQ) images of Figure 2 (USGS, 2001). The remote images are sensitive in the visible spectrum and have resolutions of 15 and 1 meters per pixel respectively. We found registration accuracy to be within the error margin of the rover’s initial position. As an additional hedge against drift in position estimation we apply a Gaussian blur operation ($\sigma = 1\text{m}$) to remove the finest

boundary details. This mitigated an occasional error in which a spectrometer sample was misplaced across a sharp unit boundary, causing a strong spectral signal that contradicted others in its unit.

A Gaussian process model (Cressie, 1991; Williams and Rasmussen, 1996; MacKay, 2003; Rasmussen and Williams, 2006) extrapolates from surface spectra and remote images to predict future abundance measurements. We describe the site of each spectrum by a vector-valued independent variable $x \in \mathbb{R}^3$ containing the site's physical position on the surface and the intensity of the image channel. We transform the latitude and longitude position $[l_{i0}, l_{i1}]$ and the satellite image pixel brightness c_i to a common scale, normalizing them to have mean zero and unit standard deviation and appending them to produce the input vector $x_i = [l_{i0}, l_{i1}, c_i]$.

Our site survey aims to recover an underlying function $f(x)$ which maps the input vector x onto the basalt abundance. Formally $f(x)$ transforms the vector-valued independent variables $x_i \in \mathbb{R}^3$ onto the scalar observations y . We presume normally-distributed observation noise ϵ and write observations of surface material as $Y = \{y_1, y_2, \dots, y_n\}$, $y_i \in \mathbb{R}$, so that $y = f(x) + \epsilon$. The mapping task predicts the true value of $f(x)$ at all locations in the exploration corridor. For unobserved sample sites X we evaluate *Maximum A Posteriori* (MAP) estimates $\hat{f}(X) = \text{argmax}_{f(X)} P(f(X)|Y)$ to produce surficial maps of any extent and resolution. Marginal prediction variance describes uncertainty about map contents, and $P(f(x)|Y)$ expresses the probability of any *combination* of future observations. Bayesian inference can fully characterize the space of possible maps given any observed data.

As a Gaussian process, $f(X)$ evaluated at a set of input points has a multivariate Gaussian distribution. A *covariance function* $\kappa(x_i, x_j)$ represents similarities between points in the input space; entries of the prior covariance matrix K are given by the covariance function for a datapoint pair: $K_{i,j} = \kappa(x_i, x_j)$, and $P(f(X)) = \mathcal{N}(0, K)$. In our model the geologic observations are perturbed by normally-distributed noise $\epsilon \sim \mathcal{N}(0, \sigma^2)$. The spectrometer observation values Y are also jointly Gaussian with the noise term contributing to the diagonal of the covariance matrix:

$$P(Y) = \mathcal{N}(0, K + \sigma^2 I) = \frac{1}{Z} e^{-\frac{1}{2} Y^T (K + \sigma^2 I)^{-1} Y} \quad (1)$$

We use the popular *squared exponential* covariance function (MacKay, 2003). Excluding the noise term the complete kernel function includes hyperparameters ψ_1, ψ_2 , and additional length scale hyperparameters w_k for each input dimension k :

$$\kappa(x_i, x_j) = \psi_1 + \psi_2 \exp \left\{ -\frac{1}{2} \sum_{k=1}^d \frac{(x_{ki} - x_{kj})^2}{w_k^2} \right\} \quad (2)$$

The standard Gaussian process prediction equations (MacKay, 2003) predict future observations from collected data. For $K_{XX'}$ representing the covariance function evaluated between the set of collected data X and future observations X' :

$$\alpha = (K_{X,X} + \sigma^2 I)^{-1} Y \quad (3)$$

$$\hat{\mu} = K_{X'X} \alpha \quad (4)$$

The system learns hyperparameters using evidence maximization (maximum likelihood fitting). Williams and Rasmussen provide details of the gradient ascent method (Williams and Rasmussen, 1996). The rover periodically re-estimates model parameters from new data, discovering spatial and cross-sensor relationships on the fly.

3.4 Utility Functions for Adaptive Exploration

Adaptive decision making requires expressing the value of new potential observations with respect to the mapping objective. For a set of candidate observation sites $A = [a_1, a_2, \dots, a_n]$ we define an objective function

$U(A)$ with reward and cost terms (Moorehead et al., 2001). The reward term $E[R(A)]$ is the expected value of a function $R(A)$ mapping collected data and associated sample sites A to a scalar value. An observation cost $L(A)$ accounts for resource requirements (like energy and time). The remote explorer chooses observations that maximize an overall utility given by $U(A) = E[R(A)] - L(A)$.

Information-theoretic reward functions value observations according to the expected reduction in the model's posterior entropy. Chaloner and Verdinelli provide an excellent review of information-driven experimental design (Chaloner and Verdinelli, 1995). Lindley first proposed to treat experimental design as maximizing a utility function based on Shannon information (Lindley, 1956; Lindley, 1972). In robotic survey applications, information gain criteria enabled the Robotic Antarctic Meteorite Search to improve rock classification decisions (Pedersen et al., 2001; Wagner et al., 2001). Single- and multi-robot systems have used information gain as an objective for mapping occupancy grids (Simmons et al., 2000; Zlot et al., 2002; Makarenko et al., 2002). Moorehead et al. expand the idea to outdoor exploration and planetary domains (Moorehead et al., 2001). These exploration strategies do not model the structure of the environment or infer future observations, but instead assign a constant information value to each unobserved location. Such metrics reduce to a measure of sensor coverage.

We represent the Amboy site as a continuous plane with discrete measurement locations. The rover chooses a subset A out of possible sampling locations V . It tries to reduce the entropy $H(V \setminus A \mid A)$ of abundance at all possible sensing sites, given all previous data (with some abuse of notation, we use the same characters to represent a set of locations and the measurements at those locations). The reward function is $R_{MAXENT}(A) = -H(V \setminus A \mid A)$. Shewry and Wynn show that under some weak assumptions one can optimize this expression by maximizing the entropy of the observations themselves (Shewry and Wynn, 1987). If we take $H(V)$ as a fixed quantity we can ignore this constant and the objective decomposes:

$$R_{MAXENT}(A) = -H(V \setminus A \mid A) = -H(V \setminus A \cup A) + H(A) \equiv H(A) \quad (5)$$

Therefore minimizing $E_A[H(V \setminus A \mid A)]$ is equivalent to maximizing observation entropy $H(A)$, a procedure known as Maximum Entropy Sampling (MES) (Ko et al., 1995; Lee, 1998; Sebastiani and Wynn, 2001; Sebastiani and Wynn, 2000). It reflects the intuitive idea that we should collect data where the result is most uncertain.

MES objectives are generally tractable for Gaussian spatial processes. For $V \in \mathbb{R}^n, V \sim \mathcal{N}(\mu, \Sigma_{V,V})$, we associate sample locations with dimensions of a multivariate Gaussian and reorder the covariance matrix to gather the observations into a block submatrix $\Sigma_{A,A}$ as in Shewry and Wynn.

$$\Sigma_{V,V} = \begin{bmatrix} \Sigma_{V \setminus A, V \setminus A} & \Sigma_{V \setminus A, A} \\ \Sigma_{A, V \setminus A} & \Sigma_{A, A} \end{bmatrix} \quad (6)$$

In traditional spatial experimental design the number of observations is constant, and MES optimization seeks sample locations to maximize the differential entropy of the marginal Gaussian $\mathcal{N}(\mu, \Sigma_{A,A})$ associated with the sub-covariance-matrix $\Sigma_{A,A}$. This quantity is proportional to a constant plus the submatrix determinant, so the reward function is a determinant maximization or d -optimal experimental design (Chaloner and Verdinelli, 1995). We have:

$$R_{MAXENT}(A) \equiv |\Sigma_{A,A}| \quad (7)$$

MES strategies have been applied to a range of spatial design problems (Cressie, 1991). Similar objective functions include the mutual information criterion (Guestrin et al., 2005), which we have applied previously to rover exploration in the context of selective data return (Thompson et al., 2008).

Optimal subset selection for conditional entropy or mutual information is an NP-complete problem (Ko et al., 1995). However, approximate solutions are adequate for many practical situations. One effective algorithm greedily maximizes the objective with each new observation (Shewry and Wynn, 1987). This approach has provable performance bounds for the mutual information criterion (Guestrin et al., 2005).

3.5 Action Selection for Intelligent Mapping

Our objective chooses paths that maximize observation entropy and satisfy constraints on end-of-day arrival time. We represent each path to the goal \mathcal{P} using interpolated waypoints $\mathcal{P} = \{\mathcal{P}_1, \mathcal{P}_2, \dots, \mathcal{P}_{\text{goal}}\}$. The associated entropy $H(\mathcal{P})$ is the joint entropy of the n observations spaced equally along the interpolated path, conditioned on all previous observations. This is only an approximation since the lower-level navigation routine might not track the interpolated path exactly. The number of sampling locations n should be large enough for an accurate approximation of future data collection. The experiments that follow use $n = 40$ for total (discretionary) path lengths up to 200m.

Movement cost is implicit in the requirement that the robot be able to reach the final goal. The cost is zero until the time budget is exhausted, but failing to reach the goal incurs infinite cost. The path planning algorithm need only explore the space of paths capable of reaching the goal. We represent this as a constrained optimization with path cost $L(\mathcal{P})$. The path cost is based on travel time with a conservative estimate of average rover velocity. Scientists specify the maximum path budget m at the outset. For a data set A of existing observations, the utility of a candidate path \mathcal{P} is based on the MES criterion:

$$U(\mathcal{P}) = H(\mathcal{P}|A) \text{ such that } L(\mathcal{P}) \leq m \quad (8)$$

We decompose the complete path into two segments - a near-term discretionary portion $\mathcal{P}_{\text{near}}$ and a fixed reserve \mathcal{P}_{far} that each receive a proportion of the total time budget. The local path planner chooses a near-term path $\mathcal{P}_{\text{near}}$ within the fixed-distance horizon (Figure 13). Execution begins with the time budget allocated evenly to segments in \mathcal{P}_{far} ; these segments and their budgets are moved to the collective discretionary portion as they fall into the rover's replanning horizon. This ensures that the rover does not linger too long in any one location, permitting short-term adaptation while enforcing an even allocation of time resources in the long term. Altering the length of the planning horizon controls the tradeoff between planning complexity and long term optimality. The local horizon path planning utility function is the following:

$$U(\mathcal{P}) = R_{\text{MAXENT}}(\mathcal{P}_a) \text{ such that } L(\mathcal{P}_a) \leq (m - L(\mathcal{P}_b)) \quad (9)$$

We will omit the subscripts for clarity in our discussion of the planning algorithm. The planner aims to find a path $\mathcal{P}_{\text{near}}$ for a time budget $m - L(\mathcal{P}_{\text{far}})$. The subpath time cost is based on the average rover velocity ν_{avg} and the Euclidean subpath lengths $l(\mathcal{P}_i)$ associated with each leg \mathcal{P}_i of the segment.

$$L(\mathcal{P}) = \nu_{\text{avg}} \sum_{\mathcal{P}_i \in \mathcal{P}} l(\mathcal{P}_i) \quad (10)$$

Path selection maximizes the joint entropy of observations in the path conditioned on all previous observations. We compute path reward from the set A' of evenly-spaced measurement locations along a path \mathcal{P} . For collected observations $A = \{a_1, \dots, a_n\}$ associated with input variables $X = \{x_1, \dots, x_n\}$, the reward function is given by the conditional covariance matrix from the Gaussian process model:

$$R_{\text{MAXENT}}(\mathcal{P}) = H(\mathcal{P}|A) \quad (11)$$

$$\equiv |\Sigma_{A', A'}| \quad (12)$$

$$\equiv |K_{A', A'} + K_{A' A}(K_{A, A} + \sigma^2 I)^{-1} K_{AA'}| \quad (13)$$

Objective: $\max_{\mathcal{P}_a} R_{\text{MAXENT}}(\mathcal{P}_a)$
 Given: existing observations A

```

GreedySelect(start, end, budget,  $\mathcal{P}_{\text{fixed}}$ )
If  $L_O(\text{start}, \text{end}) > \text{budget}$ :
    Return infeasible
Base case - no intermediate waypoints:
 $\mathcal{P} \leftarrow \{\text{start}, \text{end}\}$ 
Else:
    Initialize best  $\leftarrow -\infty$ 
    For  $b$  in splits:
        For middle in lateral offsets:
             $\mathcal{P}_1 \leftarrow \text{GreedySelect}(\text{start}, \text{middle}, b, \mathcal{P}_{\text{fixed}})$ 
             $\mathcal{P}_2 \leftarrow \text{GreedySelect}(\text{middle}, \text{end}, \text{budget} - b, \mathcal{P}_{\text{fixed}} \cup \mathcal{P}_1)$ 
            If  $H(\mathcal{P}_{\text{fixed}} \cup \mathcal{P}_1 \cup \mathcal{P}_2 | A) > \text{best}$ :
                best  $\leftarrow H(\mathcal{P}_{\text{fixed}} \cup \mathcal{P}_1 \cup \mathcal{P}_2 | A)$ 
                 $\mathcal{P} \leftarrow \mathcal{P}_1 \cup \mathcal{P}_2$ 
    Return  $\mathcal{P}$ 

```

Figure 15: Algorithm for selecting lateral offsets based on the recursive greedy method of (Chekuri and Pal, 2005) and Singh et al. (Singh et al., 2007).

The path planner generates a near-term plan $\mathcal{P}_{\text{near}}$ for the discretionary budget by considering lateral offsets for each forward position along the corridor (Figure 13). We search the space of lateral offsets using a recursive greedy path planning algorithm first formulated by Chekuri and Pal (Chekuri and Pal, 2005) and elaborated by Singh et al. (Singh et al., 2007). The algorithm evaluates each legal midpoint, breaking the path planning problem into two smaller segments. For each midpoint it evaluates several potential assignment ratios of the remaining resource budget among the halves. It calls itself recursively on the left subpath and then the right, finding the high-scoring path for the left half and then taking that portion as fixed for the purposes of finding the right half. Its branching factor is equal to the number of waypoints multiplied by the number of potential budget splits. Figure 15 outlines the procedure.

Our algorithm selects from five possible lateral offsets. For each waypoint we evaluate three potential splits that give 25%, 50%, and 75% of the budget to the first half. Candidate subpaths must never exceed the budget allocation for their segment; if there is no valid option the planner resorts to a default path driving directly to that segment’s endpoint. Thus, if the robot overspends its discretionary budget (due to navigation difficulties) it drives directly to the end of its discretionary region. The following round of planning reassigned the discretionary portions and possibly receives an additional fraction of the reserve. The rover then plans its next path based on the updated discretionary budget.

The short horizon permits fast real-time replanning; for a modern single-core laptop processor running unoptimized code the algorithm requires 5 – 30 seconds. Planning is fastest when the rover has little discretionary time remaining; pruning the non-conforming paths can dramatically reduce the search size. If the rover is behind schedule there is no time remaining in the discretionary portion, and the rover continually advances to the next middle waypoint until it catches up with the original schedule to access a later segment’s reserve allowance.

In the Amboy experiments the rover replans at 3 minute intervals, evaluating candidate paths containing 40 future observations. The rover might spend anywhere from 2 – 5 minutes planning during a 30 minute run. We aimed for a practical compromise between path optimality and computation time, such that time spent planning would “pay for itself” with more efficient rover paths.

We validated the greedy path planner by comparing its observation entropies to those of exhaustive and fixed

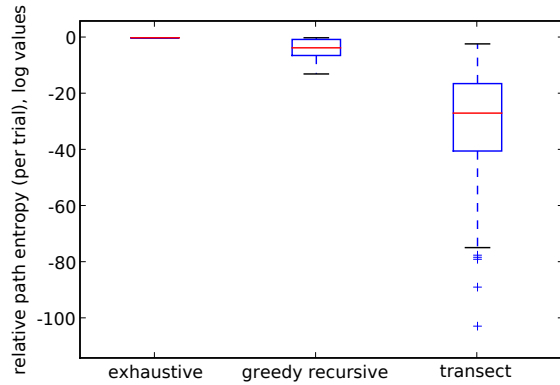


Figure 16: Comparison of path entropies for 70 planning trials using exhaustive and greedy path planning methods. Columns show path entropy relative to the optimal (exhaustive) strategy, with data quartiles, extrema, and plus signs indicating outliers.

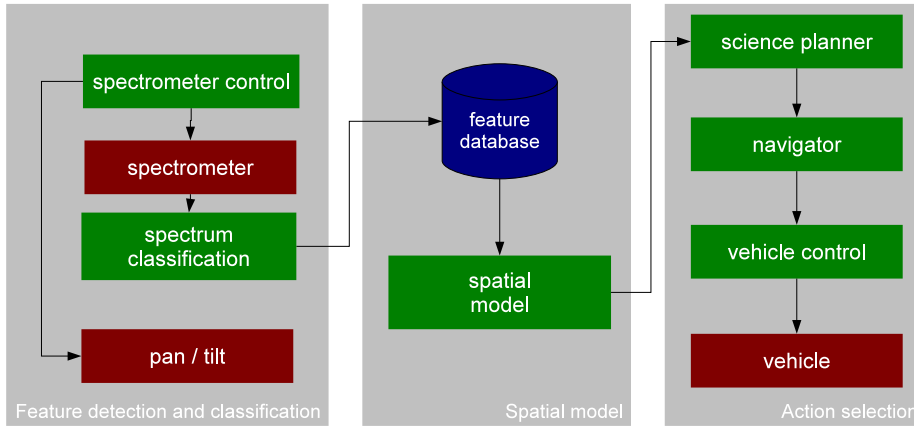


Figure 17: Components for intelligent mapping. The database of spectral features feeds into a Gaussian process spatial model. This informs information-optimal waypoint selection by the science planner module.

path selection. We performed 70 planning trials offline using data from the Amboy Crater traverses (to be described in the following section). We imposed a reasonable time budget to force the adaptive planner out of an exhaustive coverage strategy. Each trial corresponded to a specific traverse time step. We constructed a Gaussian process model and then generated a 4-waypoint path forward down the corridor. Figure 16 compares path entropy from the greedy algorithm, an exhaustive search strategy and a non-adaptive fixed transect that runs directly from the start to the end. The greedy algorithm sacrifices some performance for speed but performs significantly better than the fixed alternative.

3.6 Execution Strategy

Our path selection architecture builds on the framework for automatic rock spectroscopy (Section 2 Figure 6). A schematic diagram appears in Figure 17. Spectra are classified using the aforementioned five-band averaging followed by Principal Component Analysis (PCA). The Gaussian process model relates this value to the latitude and longitude location of each sample and the brightness of terrain in remote sensing data. A “Science Planner” then uses this model to evaluate entropies of new observations along candidate paths.

Every three minutes of travel time the Science Planner pauses to re-plan the high-level path waypoints. This time interval generally corresponds to $50 - 100m$ of forward travel, subject to delays from spectrometer calibration and low-level obstacle avoidance. The Science Planner recomputes the spectral PCA axis and re-trains Gaussian process hyperparameters. It assigns the discretionary portion of the budget to account for elapsed time.

The Science Planner chooses a path with the recursive algorithm and sends the resulting waypoints to a navigation executive. The navigation executive breaks the complete trajectory into lower-level subgoals separated by at least $30m$. It sends these subgoals to a local navigator that computes drive arcs using forward projection and D^* path planning (Singh et al., 2000; Maimone et al., 2007; Stentz and Hebert, 1995). Note that the rover does not necessarily track the ideal straight-line path between waypoints. Instead it attempts to find the closest path to the next waypoint from the rover’s current location. The Executive handles interrupt activities such as recovery maneuvers and fault handling. Finally, the Vehicle Controller module performs active motor-level control by supplying appropriate drive speeds to move the rover in the intended direction.

We set the rover’s target velocity to a fixed value of 1.0 meters per second. In practice the navigator traveled more cautiously with occasional detours to avoid rough terrain and obstacles. The Science Planner’s average velocity estimate of 0.33m/s accounted for delays due to calibration, replanning, and hazard avoidance by the Navigator. During the traverse the Spectrometer Control module acquires one new measurement every 7 seconds, corresponding roughly to a new spectrum for each $2 - 5m$ of forward progress.

3.7 Field Experiment Procedures

Amboy Crater field experiments evaluate autonomous surficial mapping of basaltic lava units with dynamic Maximum Entropy Sampling that exploits surface and orbital data. The rover begins with no prior information about correlations between data products and learns model parameters on the fly. Here we focus on the “Bonnie and Clyde” site. Figure 18 shows example paths overlayed on their resulting map reconstructions. Each circle along the path corresponds to a different spectrum. Green areas indicate a high estimated concentration of sediment while yellow indicates basalt. Paths do not always reach the end goal since our imposed time limit occasionally elapses prior to the rover’s arrival. Our test suite compares several path selection techniques:

- **Fixed, Transect:** A straight drive across the exploration corridor (Figure 18 Left).
- **Fixed, Maximum Coverage:** A static zig-zag coverage pattern to uniformly cover the exploration corridor, subject to time constraints (Figure 18 Middle Left). We alternate beginning with a right or a left turn.
- **Adaptive ASTER:** Adaptive exploration using the ASTER VIS/NIR orbital image with 15m/pixel resolution as a third input dimension. (Figure 18 Middle Right).
- **Adaptive DOQ:** Adaptive exploration using the DOQ overflight image with 1m/pixel resolution as a third input dimension (Figure 18 Right).
- **Synthetic Random:** A map that does not correspond to any physical traverse; here both pixel class labels are chosen with equal probability. This is not a practical strategy, but we use it as a control group for the experiment.
- **Synthetic Uniform:** Another synthetic map, filled with pixel labels corresponding to the predominant class. Again, we use this as a control group for our comparison.

Time budgets were 24 minutes for each physical exploration method except the trials with DOQ overflight data. Two of these DOQ trials used a budget of 30 minutes, and a third was handicapped with a budget of

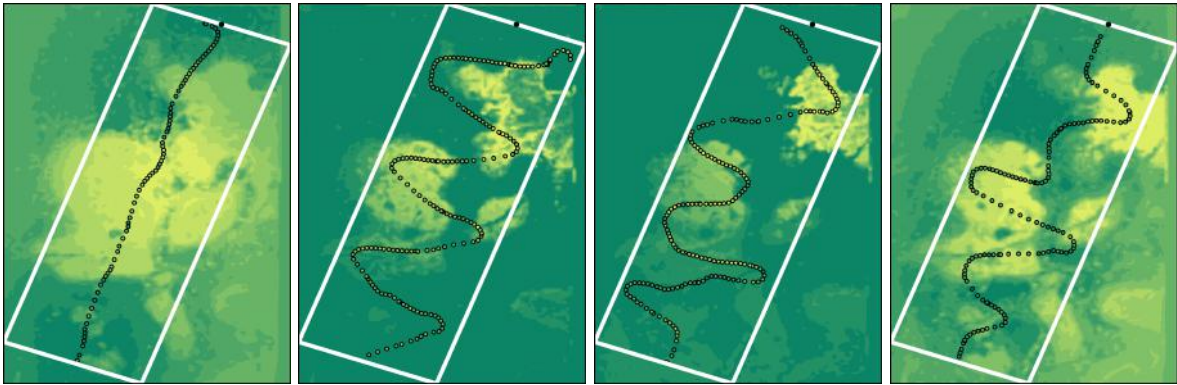


Figure 18: Examples of fixed navigation strategies with their resulting map reconstructions. Green areas indicate a high estimated concentration of sediment while yellow indicates basalt. Left: Fixed transect-based navigation. Middle Left: Fixed farming pattern for maximal coverage, subject to the same time constraints as the adaptive strategies. Middle Right: Adaptive navigation using the low-resolution ASTER image. Right: Adaptive navigation using the high-resolution DOQ image. The low-level navigator is not constrained to travel forward, and this last run evidences some backwards travel during turns and obstacle avoidance.

16 minutes. We had experimented with several alternative budgets to find one that was challenging but not impossible. We eventually found 24 minute trials to be an appropriate balance that forced the planner into interesting resource tradeoff decisions. However, the field season ended before time-equivalent DOQ tests could be completed so we encourage some caution in interpreting the statistical significance of DOQ trials.

The experimental trials began by initializing the rover position using differential GPS and calibrating the spectrometer. Each started at the same location and ended when the rover reached the far end of the corridor or the time limit elapsed. The initial plan was a straight-line drive towards the goal; after 10-20 seconds enough spectra were collected to train the spatial model and initiate the first replanning. This *tabula raza* initialization gives a fair comparison against fixed alternatives, though an actual mission would probably rely on geologist experts for an initial plan.

Variations in low-level navigation would produce different paths between runs even when the planner’s selected waypoints were identical. We took several measures to reduce inter-trial variance from these factors. We ignored trials with catastrophic mobility problems, such as a single obstacle avoidance maneuver that lasted longer than 60 seconds or a fault that required manual intervention. This occurred in about 1/3 of the trials. In general these failures were distributed evenly in proportion to the total number of obstacle-induced recovery actions.

We mitigated illumination changes by performing the tests with the sun at high elevation. The rover paused every 7 minutes to re-calibrate the spectrometer against its white reference target. This interval was a practical compromise between timely recalibration and traverse efficiency. Occasionally a calibration failed, requiring multiple successive attempts. We disregarded traverses in which the rover had two successive calibration failures or when it obviously missed the reference target and produced bad data as a result. Registration and localization error may also be responsible for some observed between-trial variance, but diagnosing this effect is subjective so we do not attempt to control for it in these tests. After our quality control measures the dataset consisted of 18 trial runs, 7 using adaptive replanning and 11 using static methods.

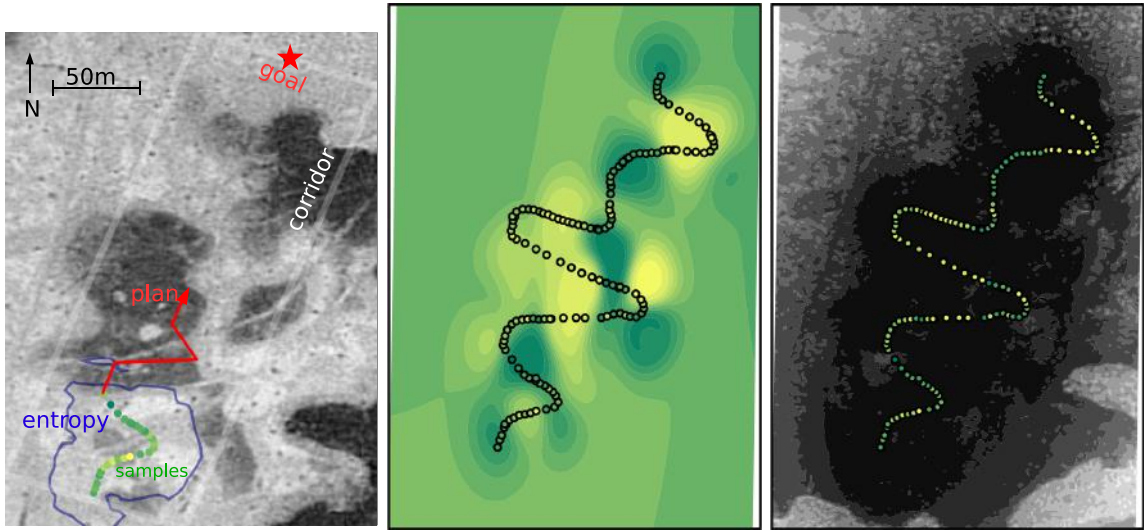


Figure 19: Left: Overflight imagery of the field site. Colored dots show spectral samples collected along the rover path. The blue line indicates one isocontour of the marginal prediction entropy. The red line shows waypoints in the current navigation plan. Center: map of surface material resulting from the traverse. Yellow signifies basalt and green signifies sediment. Right: Marginal prediction variance associated with the reconstructed map. Bright areas have high prediction uncertainty.

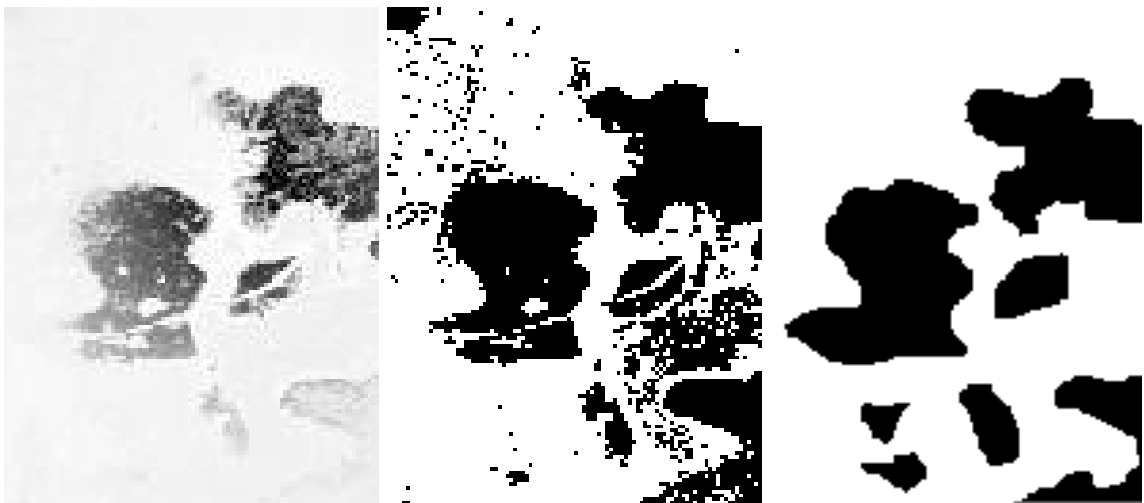


Figure 20: Left: Typical map inference result. Center: Binarized version resulting from k-means quantization. Right: Manual ground truth labeling of basalt and sediment terrain types.

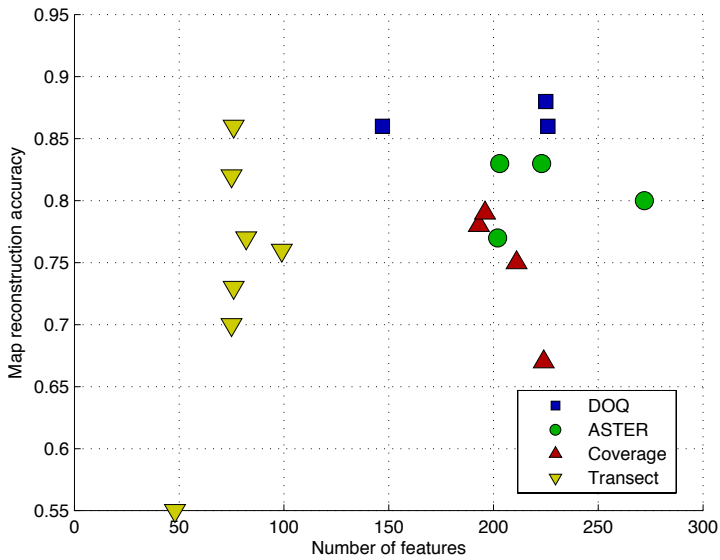


Figure 21: Results of the experimental trials from Amboy Crater: the number of spectral samples (features) collected in each run and the pixel-wise accuracy of the reconstructed binary classification map. We compare four methods: adaptive traverses based on high-resolution DOQ images, adaptive traverses based on ASTER images, and static control cases using straight-line transects and maximum-coverage patterns. The adaptive methods generally produce more accurate maps for runs with similar numbers of measurements.

3.8 Field Test Results

Figure 19 shows a typical trial in which the rover traveled 0.46 kilometers. This trial used the adaptive DOQ method and lasted approximately 24 minutes. The rover chose a pattern that balanced the diversity of visited surface units against overall spatial coverage. The rightmost column shows remote imagery of the traverse area. Here the rover is several minutes into its traverse; it has collected 27 spectral samples and planned a four-segment path illustrated in red. The Science Planner chooses a path that covers the main surficial units while respecting the time budget. The blue line indicates one isocontour of the marginal prediction variance; it is tantamount to a frontier along which map predictions are equally certain. In this timestep the entropy of the black basalt is higher than its physical proximity would suggest because the patch is still distant along the third dimension of image intensity. The center column shows the inferred map using yellow for basalt and green for clay sediment as before.

The rightmost column illustrates the end-of-traverse uncertainties with bright values corresponding to regions of high predictive variance. The model prediction is less certain in areas that are far from the rover path and more accurate within the corridor. The unvisited basalt patch at lower right is highly uncertain because it is dissimilar to collected data with respect to both location and image pixel values.

Our performance metric measures the fidelity of the reconstructed map. We retrain a Gaussian process model with all measurements and binarize the result into two geologic types with k-means vector quantization. Figure 20 shows one example of the inferred map and the resulting binary classification. We compare the reconstruction to a ground-truth map from a manually labeled DOQ image. This yields a pixel-wise classification accuracy score for each reconstructed map.

Table 2 shows performance statistics resulting from 18 trials in this traverse area. We report p-values from a one-tailed T-test (Casella and Berger, 2002) against the hypothesis that performance is equivalent to a

Method	Accuracy (std)	# Spectra (std)	p-value (n)
Adaptive (DOQ)			
Trial 1	0.86	226	
Trial 2	0.88	225	
Trial 3	0.86	147	
Total	0.87 (0.01)	199.3 (45.3)	<0.01 (3)
Adaptive (ASTER)			
Trial 1	0.80	272	
Trial 2	0.77	202	
Trial 3	0.83	203	
Trial 4	0.83	223	
Total	0.81 (0.03)	225.0 (32.8)	<0.05 (4)
Fixed (Coverage)			
Trial 1	0.75	211	
Trial 2	0.78	193	
Trial 3	0.79	196	
Trial 4	0.67	224	
Total	0.75 (0.05)	206.0 (14.4)	n/a (4)
Fixed (Transect)			
Trial 1	0.82	75	
Trial 2	0.55	48	
Trial 3	0.77	82	
Trial 4	0.70	75	
Trial 5	0.73	76	
Trial 6	0.76	99	
Trial 7	0.86	76	
Total	0.74 (0.09)	75.9 (15.0)	0.45 (7)
Synthetic (Uniform)			
Total	0.57 (< 0.01)	n/a	0 (5)
Synthetic (Random)			
Total	0.50 (< 0.01)	n/a	<0.01 (5)

Table 2: Results of the Amboy Crater Traverses: map reconstruction accuracy, given as the fraction of pixels which are labeled correctly; the average number of spectra collected during each experimental run; and the p-value of a one-tailed T-test against the methods' equivalence to a fixed coverage pattern.

Method	Time in basalt (std)	Crossings (std)	Crossing rate (std)	p-value (n)
Adaptive				
DOQ	60% (2%)	14 (4)	0.08 (0.01)	0.04 (3)
ASTER	56% (9%)	11 (2)	0.05 (0.01)	0.76 (4)
Fixed				
Coverage	48% (9%)	10 (3)	0.05 (0.02)	n/a (4)
Transect	53% (15%)	6 (1)	0.08 (0.02)	0.04 (7)

Table 3: Boundary crossing behavior during the Amboy traverses. The second column lists the fraction of traverse time spent on basalt platform units as determined by hand-labeled orbital imagery. The third column shows the number of times the rover entered or exited a basalt platform. The fourth column shows the proportion of boundary crossings as a fraction of the total number of observations. Finally we provide the p-value of a one-tailed T-test against the crossing rate’s equivalence to a fixed coverage pattern.

static coverage pattern. This table and Figure 21 show the number of features (collected spectra) for each run and the resulting reconstruction accuracy. In general the adaptive methods outperform static methods which in turn outperform the uniform and random cases.

The adaptive traverses based on DOQ overflight data perform best. The DOQ trials are subject to the timing issues mentioned above, but we still report this data for several reasons. The low variance among the DOQ accuracy implies that the time budgets were not different enough to pose a clear handicap or advantage. Moreover, due to navigation irregularities between runs, the average number of measurements collected was actually *smaller* in DOQ trials than in the fixed coverage trials. The coverage patterns happened to drive through open terrain, resulting in fewer obstacle-induced pauses.

Several trends are evident. First, both adaptive methods outperform static coverage patterns ($\alpha = 0.05$). The variance in the number of collected spectra is greater for adaptive methods than for fixed methods, representing a greater variety in path choice. However, the overall accuracy variance is reduced which may reflect adaptation to navigation delays. Attention to the remote sensing image ensures that the rover sees representative samples of the distinct terrain units without missing significant basalt patches. Half of the fixed coverage patterns miss the final basalt patch (Figure 18), but all the adaptive methods visit this area. Adaptive methods generally avoid homogeneous areas of sediment such as the Southeast and Northwest corners of the corridor. Instead the rover learns to confidently infer this surface material from the overflight image.

Finally, Maximum Entropy Sampling prefers regions of high change such as transitions across basalt mounds. Adaptive path planning using high-resolution orbital data crosses boundaries at a significantly higher rate than the fixed coverage pattern. This produces a higher number of samples near boundary regions. In other words, adaptive sampling from orbital data permits extrapolation within each unit, making additional samples from the interiors redundant. As a result the adaptive methods spend more time in basalt patches (Table 3).

An adaptive sampling option can also be a useful hedge against execution uncertainty. It can recover from mobility faults by computing alternative plans. It can also exploit unexpected new features or resource surpluses. Trials containing serious navigation errors illustrate this effect, even though we exclude them from the performance statistics. Consider the traverse in Figure 22. Here a group of bushes blocked the intended route and obstacle avoidance maneuvers delayed the rover for several minutes. The next replanning cycle compensated with a revised path. It chose a truncated coverage pattern shown in Figure 22 (Right).

These experiments demonstrate automated mapping for automated kilometer scale site survey. The rover begins with no *a priori* knowledge of surface materials. Instead it discovers the relevant distinctions and improves its exploration efficiency by leveraging spatial trends and correlations with remote sensing. The end-of-traverse time and position constraints permit integration into mixed mission plans that include pre-

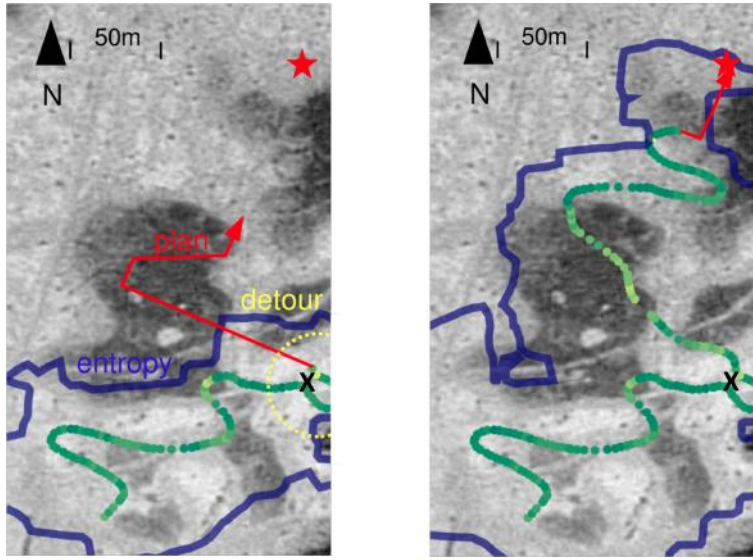


Figure 22: Recovery from navigation errors. Left: In this run, a navigation error delayed the rover for several minutes. The location of the obstacle is marked with a dark “X.” Right: The subsequent replanning cycle adapted to the situation by computing an alternative path that accommodated the delay.

scripted sampling and navigation waypoints. Scientists traversing to a new site could use corridor exploration for limited science autonomy *en route*.

4 Conclusions

The Amboy field experiment shows foundational capabilities for Science on the Fly. The rover system demonstrates feature targeting and instrument control, detecting relevant science features in images, calibrating and targeting a reflectance spectrometer. It builds a map of unique physical features, interprets spectra and recovers the principal distinctions in surface material over kilometer scales. The rover uses this data to predict the science value of future measurement locations. It learns spatial structure in the environment, reinterprets orbital data in light of surface observations, and plans informative paths that make the best use of limited time resources. Among the specific contributions of this research are the following:

- Strategies for automatic rock detection, tracking, and instrument targeting with a catalog of unique features discovered during a transect.
- Methods for automatic interpretation of rover reflectance spectra
- Information-driven approaches that adaptively plan paths and construct surficial maps on kilometer scales
- A Gaussian process model that incorporates spatial- and cross-sensor relationships, reinterpreting collected data and orbital observations during travel.
- A real time experiment in the field with noisy data.

We do not intend our mapping objective to be a universal standard of science value. In particular it disregards the potential of novel features to inspire new interpretations or invalidate assumptions of the underlying spatial model. We emphasize representative sampling of the environment rather than detecting

novel outliers or seeking specific high-value targets. Such mission objectives would favor different science value formulations and planning methods. In general we find spatial models to be a powerful tool for remote exploration. They provide a principled means for adaptive decision making that incorporates multiple sensing modes.

There are several promising avenues for future work in feature detection and classification. Richer models of surface morphology could use explicit image segmentation into different surface types. Classification decisions could incorporate multiple complementary sensors as in the work of Pedersen (Pedersen, 2000). Judicious deployment is important for these large instrument suites, and some highly informative sensors require long integration times. Feature classification offers a chance to incorporate more specialized geologic knowledge, both in the interpretation of spectroscopic data and image analysis (Dunlop et al., 2007; Estlin et al., 2009).

Future work might consider changes in the action selection routines. It might be advantageous to formulate path cost in terms of cost per unit time rather than a hard “end-of-day” position constraint. With this alternate formulation the loss is directly proportional to plan execution time (Moorehead, 2001). It would also be useful to introduce some notion of navigability into the high-level path planning routine, or to provide more flexibility in possible paths.

Finally, Science on the Fly could apply to other platforms and exploration environments. One-dimensional models such as time series are relevant to temporal subsampling, such as in spacecraft flybys, lander image sequences, or engineering imagery from spacecraft maneuvers. Two-dimensional spatial models have obvious applicability for mobile surface exploration, but also aerial remote sensing from balloons, airships, and gliders (Hayden et al., 2010; Fink et al., 2005; Noor et al., 2007).

The science return of planetary exploration missions is determined not only by the instrument suite, but also by limits to time, energy and bandwidth resources. Long range *over-the-horizon* travel by surface rovers is a poignant example. Here onboard data understanding can play a useful role in navigation and instrument deployment. Adaptive mapmaking using detected features provides a natural framework for determining science value by combining prior expectations with discovered trends. Principled autonomy solutions will be increasingly important for outer planets missions where our advance understanding is weak and communication is even more constrained.

Acknowledgments

The authors wish to thank Dom Jonak for his indispensable technical expertise in rover navigation, logistics, and photography. Thanks to Reid Simmons for help and advice with planning aspects, and to Jeff Schneider for his help with formulating the spatial models and exploration strategy. Steve Chien provided counsel in operations modes and questions of science value. Thanks to James Teza for his assistance in data collection. Ron Greeley and Shelby Cave (Arizona State University) provided assistance in site selection. Many thanks to Phil Christensen for his understanding of the site. Rebecca Castaño and the JPL AEGIS / OASIS team gave advice and inspiration. The rock detection software draws heavily on publicly-available code from the Intel OpenCV libraries, courtesy Intel Co. and Gary Bradski. This work was funded through NASA ASTEP Grant #NNG0-4GB66G “Science on the Fly” and performed at Carnegie Mellon University. Copyright 2011 California Institute of Technology. All Rights Reserved. U.S. Government Support Acknowledged.

References

ASD, Inc. (2010). <http://www.asdi.com/>.

Bajracharya, M., Diaz-Calderon, A., Robinson, M., and Powell, M. (2005). Target tracking, approach, and

- camera handoff for automated instrument placement. IEEE Aerospace Conference Proceedings, Big Sky, Montana, pages 52–59.
- Bornstein, B. and Castaño, R. (2005). Creation and testing of an artificial neural network based carbonate detector for mars rovers. IEEE Aerospace Conference Proceedings, Big Sky, Montana.
- Cabrol, N. A., Wettergreen, D., Warren-Rhodes, K., Grin, E. A., et al. (2007). Life in the Atacama: Searching for Life with Rovers. Journal of Geophysics Research, 112:G04S02.
- Calderón, F., Thompson, D. R., and Wettergreen, D. (2008). Autonomous Rover Reflectance Spectroscopy with Dozens of Targets. The International Symposium on Artificial Intelligence, Robotics and Automation in Space (i-SAIRAS).
- Calderón, F. J. (2007). Autonomous Reflectance Spectroscopy by a Mobile Robot for Mineralogical Characterization. Masters Thesis, Carnegie Mellon Robotics Institute, CMU-RI-TR-07-46.
- Carsten, J., Rankin, A., Ferguson, D., and Stentz, A. T. (2007). Global Path Planning on-board the Mars Exploration Rovers. IEEE Aerospace Conference.
- Casella, G. and Berger, R. (2002). Statistical inference. Duxbury.
- Castaño, R. (2006). Personal communication.
- Castaño, R., Estlin, T., Gaines, D., Chouinard, C., Bornstein, B., Anderson, R. C., Burl, M., Thompson, D. R., CAstaño, A., and Judd, M. (2007). Onboard autonomous rover science. IEEE Aerospace Conference Proceedings, Big Sky, Montana.
- Chaloner, K. and Verdinelli, I. (1995). Bayesian Experimental Design: A Review. Statistical Science, 10(3):273–304.
- Chekuri, C. and Pal, M. (2005). A Recursive Greedy Algorithm for Walks on Directed Graphs. IEEE Symposium on the Foundations of Computer Science.
- Cheng, Y., Maimone, M., and Matthies, L. (2006). Visual odometry on the Mars exploration rovers-a tool to ensure accurate driving and science imaging. Robotics & Automation Magazine, IEEE, 13(2):54–62.
- Chien, S., Sherwood, R., Tran, D., Cichy, B., G., C. R., Castaño, R., Davies, A., Mandl, D., Frye, S., Trout, B., et al. (2005). Using Autonomy Flight Software to Improve Science Return on Earth Observing One. Journal of Aerospace Computing, Information, and Communication, 2:196–216.
- Christian, D. A., Wettergreen, D., Bualat, M., Schwehr, K., Tucker, D., and Zbinden, E. (1997). Field experiments with the ames marsokhod rover. Proceedings of the Conference on Field and Service Robotics (FSR).
- Cressie, N. A. (1991). Statistics for Spatial Data. Wiley and Sons, New York.
- Deans, M., Wettergreen, D., and Villa, D. (2005). A Sun Tracker for Planetary Analog Rovers. The International Symposium on Artificial Intelligence, Robotics and Automation in Space (i-SAIRAS), page 76.
- Diggles, P. J. (2003). Statistical Analysis of Spatial Point Patterns. Arnold Publishers, London.
- Dunlop, H., Thompson, D. R., and Wettergreen, D. (2007). Multi-scale Features for Detection and Segmentation of Rocks in Mars Imagery. IEEE Conference on Computer Vision and Pattern Recognition (CVPR).
- Estlin, T., Bornstein, B., Gaines, D., Thompson, D. R., Castaño, R., Anderson, R. C., de Granville, C., Burl, M., Judd, M., and Chien, S. (2010). AEGIS Automated Targeting for the MER Opportunity Rover. International Symposium on Artificial Intelligence, Robotics, and Automation in Space (i-SAIRAS).

- Estlin, T., Castaño, R., Bornstein, B., Gaines, D., Anderson, R. C., de Granville, C., Thompson, D. R., Burl, M., Judd, M., and Chien, S. (2009). Automated Targeting for the MER Rovers. *AIAA Aerospace*.
- Estlin, T., Gaines, D., Nesnas, I., Castaño, R., Bornstein, B., Judd, M., and Anderson, R. C. (2008). Autonomous Science and Commanding for a Mars Rover. *International Symposium on Artificial Intelligence, Robotics, and Automation in Space (i-SAIRAS)*.
- Fink, W. (2006). Generic prioritization framework for target selection and instrument usage for reconnaissance mission autonomy. In *Neural Networks, 2006. IJCNN'06. International Joint Conference on*, pages 5367–5370. IEEE.
- Fink, W., Datta, A., Dohm, J., Tarbell, M., Jobling, F., Furfarro, R., Kargel, J., Schulze-Makuch, D., and Baker, V. (2008). Automated Global Feature Analyzer-A Driver for Tier-Scalable Reconnaissance. *IEEE Aerospace Conference, Big Sky, Montana*, pages 1–12.
- Fink, W., Dohm, J., Tarbell, M., Hare, T., and Baker, V. (2005). Next-generation robotic planetary reconnaissance missions: a paradigm shift. *Planetary and Space Science*, 53(14-15):1419–1426.
- Fong, T. W., Allan, M., Boussounouse, X., Bualat, M. G., Deans, M., Edwards, L., Flckiger, L., Keely, L., Lee, S. Y., Lees, D., To, V., and Utz, H. (2008). Robotic Site Survey at Haughton Crater. *International Symposium on Artificial Intelligence, Robotics, and Automation in Space (i-SAIRAS)*.
- Fox, J., Castaño, R., and Anderson, R. C. (2002). Onboard autonomous rock shape analysis for mars rovers. *IEEE Aerospace Conference Proceedings, Big Sky, Montana*.
- Furfarro, R., Dohm, J., Fink, W., Kargel, J., Schulze-Makuch, D., Fairén, A., Palmero-Rodriguez, A., Baker, V., Ferré, P., Hare, T., et al. (2008). The search for life beyond Earth through fuzzy expert systems. *Planetary and Space Science*, 56(3-4):448–472.
- Furfarro, R., Kargel, J., Lunine, J., Fink, W., and Bishop, M. (2010). Identification of cryovolcanism on Titan using fuzzy cognitive maps. *Planetary and Space Science*, 58(5):761–779.
- Greeley, R. and Iversen, J. D. (1978). Field Guide to Amboy Lava Flow, San Bernardino County, California. *Aeolian Features of Southern California: A Comparative Planetary Geology Guidebook*.
- Guestrin, C., Krause, A., and Singh, A. (2005). Near-optimal Sensor Placements in Gaussian Processes. *Proceedings of the International Conference on Machine Learning (ICML)*.
- Gulick, V. C., Morris, R. L., Ruzon, M. A., and Roush, T. L. (2001). Autonomous image analysis during the 1999 marsokhod rover field test. *Journal of Geophysical Research*, 106(E4):7745–7764.
- Hartley, R. and Zisserman, A. (2004). *Multiple View Geometry in Computer Vision*. Cambridge Univ. P., 2nd ed. edition.
- Hatheway, A. W. (1971). *Lava Tubes and Collapse Depressions*. PhD thesis. Amboy map reprinted in Greeley 1978.
- Hayden, D., Chien, S., Thompson, D., and Castano, R. (2010). Using Onboard Clustering to Summarize Remotely Sensed Imagery. *IEEE Intelligent Systems*, 25:3:86–91.
- Huntsberger, T., Cheng, Y., Stroupe, A., and Aghazarian, H. (2005). Closed loop control for autonomous approach and placement of science instruments by planetary rovers. *IEEE Conference on Intelligent Robots and Systems (IROS)*.
- Hutchinson, S. A., Hager, G. D., and Corke, P. I. (1996). A tutorial on visual servo control. *IEEE Trans. Robotics and Automation*, 12(5):651–670.
- Kean, S. (2010). Making Smarter, Savvier Robots. *Science*, 329(5991):508.
- Ko, C. W., Lee, J., and Queyranne, M. (1995). An Exact Algorithm for Maximum Entropy Sampling. *Operations Research*, 43(4):684–691.

- Lee, J. (1998). Constrained maximum-entropy sampling. *Operations Research*, 46:5:655–664.
- Lindley, D. (1956). On the measure of information gain provided by an experiment. *Ann. Math. Statistics*, 27:199–218.
- Lindley, D. (1972). *Bayesian statistics*. Society for Industrial and Applied Mathematics Philadelphia.
- Lowe, D. (2004). Distinctive Image Features from Scale-Invariant Keypoints. *International Journal of Computer Vision (IJCV)*, 60(2):91–110.
- MacKay, D. C. J. (2003). *Information Theory, Inference, and Learning Algorithms*. Cambridge University Press, Cambridge, UK.
- Madison, R. (2006). Improved target handoff for single cycle instrument placement. *IEEE Aerospace Conference Proceedings, Big Sky, Montana*.
- Maimone, M., Leger, P., and Biesiadecki, J. (2007). Overview of the Mars Exploration Rovers Autonomous Mobility and Vision Capabilities. *IEEE International Conference on Robotics and Automation (ICRA)*.
- Makarenko, A., Williams, S., Bourgault, F., and Durrant-Whyte, H. (2002). An experiment in integrated exploration. *Proceedings of the IEEE International Conference on Intelligent Robots and Systems (IROS)*, pages 534–539.
- McGuire, P., Orm  , J., Mart  nez, E., Manfredi, J., Elvira, J., Ritter, H., Oesker, M., and Ontrup, J. (2005). The Cyborg Astrobiologist: first field experience. *International Journal of Astrobiology*, 3(03):189–207.
- Moorehead, S. (2001). *Autonomous Surface Exploration for Mobile Robots*. PhD thesis, Robotics Institute, Carnegie Mellon University, Pittsburgh, PA.
- Moorehead, S., Simmons, R., and Whittaker, W. (2001). A multiple information source planner for autonomous planetary exploration. *International Symposium on Artificial Intelligence, Robotics and Automation in Space (i-SAIRAS)*.
- Mustard, J. F., Pieters, C. M., and Pratt, S. F. (1986). Deconvolution of spectra for intimate mixtures. *Lunar and Planetary Sciences Conference (LPSC)*.
- Noor, A., Cutts, J., and Balint, T. (2007). Platforms for discovery: exploring Titan and Venus. *Aerospace America*, 45(6):32.
- P. Backes et al. (2005). Automated rover positioning and instrument placement. *IEEE Aerospace Conference Proceedings, Big Sky, Montana*.
- Pedersen, L. (2000). *Robotic Rock Classification and Autonomous Exploration*. PhD thesis, Robotics Institute, Carnegie Mellon University, Pittsburgh, PA.
- Pedersen, L. (2002). Science target assessment for mars rover instrument deployment. *IEEE Conference on Intelligent Robotics and Systems (IROS)*, 1:817–822.
- Pedersen, L., Deans, M., Lees, D., Rajagopalan, S., and Smith, D. E. (2005). Multiple target single cycle instrument placement. *International Symposium on Artificial Intelligence, Robotics and Automation in Space (i-SAIRAS)*.
- Pedersen, L., Wagner, M. D., Apostolopoulos, D., and Whittaker, W. R. L. (2001). Autonomous robotic meteorite identification in antarctica. *IEEE International Conference on Robotics and Automation (ICRA)*.
- Pugh, S., Barnes, D., Pullan, D., and Tyler, L. (2010a). Knowledge based science target identification system (kstis). *International Symposium on Artificial Intelligence, Robotics and Automation in Space (i-SAIRAS)*.

- Pugh, S., Tyler, L., and Barnes, D. (2010b). Automatic pointing and image capture (apic) for exomars type mission. International Symposium on Artificial Intelligence, Robotics and Automation in Space (i-SAIRAS).
- Ramsey, M. and Christensen, P. (1998). Mineral abundance determination- Quantitative deconvolution of thermal emission spectra. Journal of Geophysical Research, 103(B1):577–596.
- Rasmussen, C. E. and Williams, C. K. I. (2006). Gaussian Processes for Machine Learning. MIT Press.
- Sebastiani, P. and Wynn, H. (2001). Experimental design to maximize information. AIP Conference Proceedings Workshop on Bayesian Inference and Maximum Entropy Methods in Science and Engineering, 568:192–203.
- Sebastiani, P. and Wynn, H. P. (2000). Maximum Entropy Sampling and Optimal Bayesian Experimental Design. Journal of the Royal Statistical Society.
- Shewry, M. and Wynn, H. (1987). Maximum Entropy Sampling. Journal of Applied Statistics, 14(2).
- Simmons, R., Apfelbaum, D., Burgard, W., Fox, M., an Moors, D., Thrun, S., and Younes, H. (2000). Coordination for multi-robot exploration and mapping. Proceedings of the AAAI National Conference on Artificial Intelligence (AAAI).
- Singh, A., Krause, A., Guestrin, C., Kaiser, W., and Batlin, M. (2007). Efficient Planning of Informative Paths for Multiple Robots. International Joint Conference on Artificial Intelligence (IJCAI).
- Singh, S., Simmons, R., Smith, T., Stentz, A., Verma, V., Yahja, A., and Schwehr, K. (2000). Recent Progress in Local and Global Traversability for Planetary Rovers. IEEE Conference on Robotics and Automation (ICRA).
- Smith, T., Thompson, D. R., and Wettergreen, D. (2007a). Generating exponentially smaller pomdp models using conditionally irrelevant variable abstraction. International Conference on Planning and Scheduling (ICAPS).
- Smith, T., Thompson, D. R., Wettergreen, D., Cabrol, N., Warren-Rhodes, K., and Weinstein, S. (2007b). Life in the Atacama: Autonomous Science for Improved Data Quality. Journal of Geophysical Research, 112:G04S03.
- Squyres, S., Arvidson, R., Baumgartner, E., Bell III, J., Christensen, P., Gorevan, S., Herkenhoff, K., Klingelh
"ofer, G., Madsen, M., Morris, R., et al. (2003). Athena Mars rover science investigation. Journal of Geophysical Research, 108(E12):8062.
- Stentz, A. and Hebert, M. (1995). A complete navigation system for goal acquisition in unknown environments. Autonomous Robots, 2(2):127–145.
- Thompson, D., Smith, T., and Wettergreen, D. (2008). Information-optimal selective data return for autonomous rover traverse science and survey. IEEE International Conference on Robotics and Automation (ICRA), pages 968–973.
- Thompson, D. R. and Castaño, R. (2007). A performance comparison of rock detection algorithms for autonomous geology. IEEE Aerospace Conference Proceedings, Big Sky Montana.
- Thompson, D. R. and Wettergreen, D. (2008). Intelligent Maps for Autonomous Kilometer-Scale Science Survey. International Symposium on Artificial Intelligence, Robotics, and Automation in Space (i-SAIRAS). Pasadena, California.
- USGS (2001). United States Geological Survey, Digital Orthophoto Quadrangles Fact Sheet 057-01. available at <http://erg.usgs.gov/ib/pubs/factsheets/fs05701.html>.

- Viola, P. and Jones, M. (2001). Rapid object detection using a boosted cascade of simple features. IEEE Conference on Computer Vision and Pattern Recognition (CVPR), 1:511–518.
- Wagner, M. D., Apostolopoulos, D., Shillcutt, K., Shamah, B., Simmons, R. G., and Whittaker, W. (2001). The science autonomy system of the nomad robot. International Conference on Robotics and Automation (ICRA), 2:1742–1749.
- Wagner, M. D., Heys, S., Wettergreen, D., Teza, J., Apostolopoulos, D., Kantor, G., , and Whittaker, W. (2005). Design and Control of a Passively Steered, Dual Axle Vehicle. 8th International Symposium on Artificial Intelligence, Robotics and Automation in Space.
- Waterhouse, S. (1997). Classification and Regression using Mixtures of Experts. Jesus College, Cambridge and Department of Engineering, University of Cambridge.
- Wettergreen, D., Cabrol, N., Baskaran, V., Calderon, F., Heys, S., Jonak, D., Luders, R., Pane, D., Smith, T., Teza, J., Tompkins, P., Villa, D., Williams, C., and Wagner, M. (2005). Second experiments in the robotic investigation of life in the atacama desert of chile. The International Symposium on Artificial Intelligence, Robotics and Automation in Space (i-SAIRAS).
- Wettergreen, D., Wagner, M., Jonak, D., Baskaran, V., Deans, M., Heys, S., Pane, D., Smith, T., Teza, J., Thompson, D., et al. (2008). Long-distance autonomous survey and mapping in the robotic investigation of life in the atacama desert. The International Symposium on Artificial Intelligence, Robotics and Automation in Space (i-SAIRAS).
- Williams, C. and Rasmussen, C. (1996). Gaussian Processes for Regression. Advances in Neural Information Processing Systems, 8:514–520.
- Winterholler, A., Roma, M., Hunt, T., and Miller, D. (2005). Design of a High-Mobility Low-Weight Lunar Rover. The International Symposium on Artificial Intelligence, Robotics and Automation in Space (i-SAIRAS), page 4.1.
- Yoder, J. and Seelinger, M. (2008). Long-range autonomous instrument placement. Experimental Robotics.
- Zlot, R., Stentz, A., Dias, M., and Thayer, S. (2002). Multi-robot exploration controlled by a market economy. Proceedings of the International Conference on Robotics and Automation (ICRA), 3.